2016

Stretch Feedback in the Lobster Heart: Experimental and Computational Analysis

Katelyn J. Suchyta
Bowdoin College, katelyn.suchyta@gmail.com

STRETCH FEEDBACK IN THE LOBSTER HEART: EXPERIMENTAL AND COMPUTATIONAL ANALYSIS

AN HONORS PAPER FOR THE DEPARTMENT OF MATHEMATICS

BY KATELYN J. SUCHYTA

BOWDOIN COLLEGE, 2016

Contents

List of Figures

Part 1. Experimental

1. Introduction

1.1. Central Pattern Generators (CPGs).

Organisms produce rhythmic behaviors through neural networks known as central pattern generators (CPGs), which control rhythmic motor behaviors, such as walking, breathing, and chewing [24, 9]. These complex behaviors can be modulated at multiple levels, including the pattern generator itself, sensory feedback, and the response of the muscle to a given pattern of motor output [10]. Understanding how these CPGs alter in response to external and internal modulation and feedback has been an important goal in the field of biology and neuroscience.

Due to the intricacies of CPG systems in complex nervous systems, including those of humans, simple CPG systems can be studied to gain an understanding of the cellular and network basis of rhythmic motor patterns. It is usually more tractable to study simpler CPG systems in invertebrate to gain an understanding of the cellular and network basis. Specifically, the heart of crustaceans can be extensively studied with detailed investigations because they are easily maintainable in vitro and electrical activity can be recorded from their identifiable neurons. The heart of the American lobster, *Homarus americanus*, is neurogenic, meaning the beating contractions are initiated by their simple CPG, the cardiac ganglion (CG). This system may provide an understanding of the rhythmic pattern regulation of a CPG system, which can then be generalized to more complex nervous systems.

1.2. Cardiac Ganglion (CG) of *Homarus Americanus*.

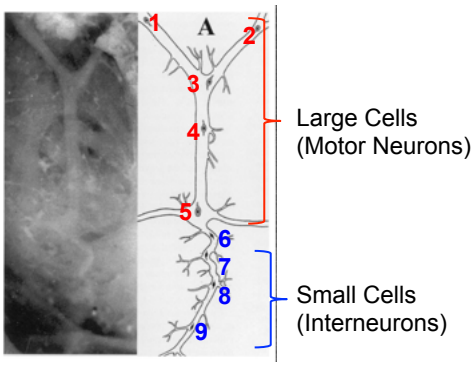

Figure 1. Schematic overview of lobster cardiac ganglion anatomy. View from dorsal side. The letter A indicates the anterior end.

Alexandrowicz (1932) initially described the CG of *H. americanus*, showing that it contains nine neurons. Among these nine neurons are four small interneurons located at the posterior end of the CG. The axons from each neuron follows a unique path through the neuropil of the CG, forming a distinct Y-shaped branch in the inner dorsal wall of the single-chamber heart as shown in **Figure 1**. The four small neurons act as pacemakers, initiating rhythmic output that initiate the activity of the five larger motor neurons at the anterior end of the CG. The large neurons produce bursts of action potentials responsible for heart muscle contractions via the neuromuscular junction. These nine cells are both electrically and chemically coupled, allowing

them to operate as a cohesive unit and fire in synchrony. This burst pattern can be maintained without any sensory inputs. Therefore, when the lobster heart is isolated, the CG continues to innervate the heart muscles in much the same way it does in the intact animal. Additionally, under a dissection microscope, the somas of the large cells (but not the small cells) are visible in isolated CG preparations, allowing their electrical activity to be recorded. Therefore, the lobster CG is amenable to experimental manipulation and can be used as a model of more complex CPG-effector systems [19, 2, 3, 31].

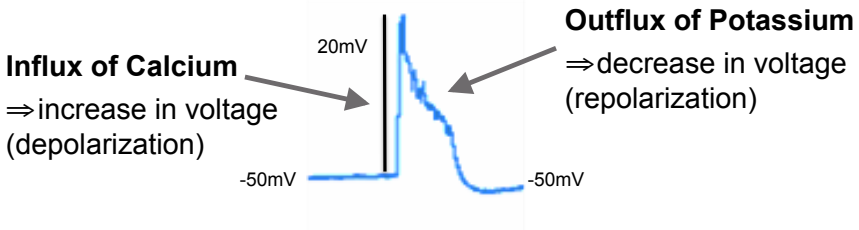

FIGURE 2. Driver potential generated by a motor neuron.

The rhythmic output of the CG originates with each neuron generating driver potentials, which are slow, sustained, and regenerative depolarizations. These driver potentials are the result of interactions of calcium currents with potassium currents [43, 44, 45]. The calcium channels allow an influx of calcium ions, resulting in depolarizations. The potassium currents cause repolarization and the return to the original resting membrane potential. Therefore, the amplitude and duration of driver potentials vary based on the balances of calcium and potassium currents, as shown in **Figure 2**, above [20, 35].

In a relatively undamaged neuron, the resting membrane potential (the membrane potential between the driver potential bursts) is around -50mV and its driver potential has an amplitude of about 20mV and occur regularly at a rate of about 20-50 per minute. The depolarizations of the driver potentials initiate bursts of action potentials, which travel down the axons to the muscles, causing the heart to contract. The driver potentials of the cardiac ganglion are coordinated and occur simultaneously in all cells [6].

1.3. **Feedback within the CPG-effector system.**

The lobster's CG is subject to extensive modulations from a variety of neuromodulators, which have a variety of effects on the rhythmic pattern of the lobster's heart contractions, as shown by the pink arrows in **Figure 3**, below.

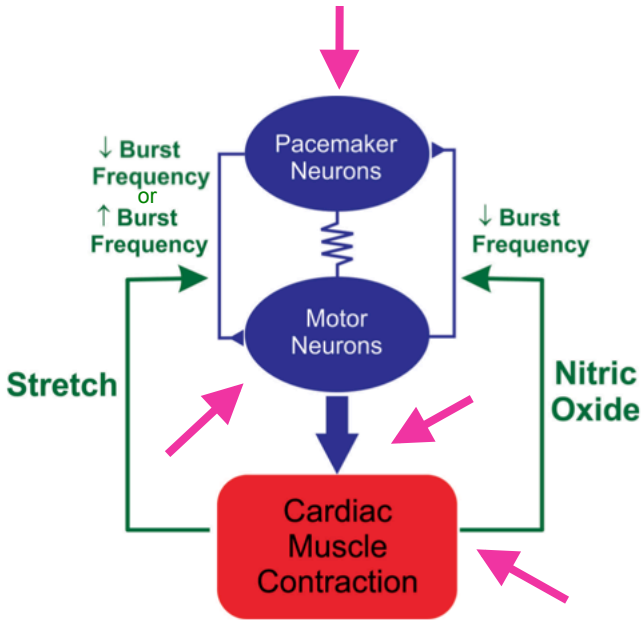

FIGURE 3. Control of the lobster CG.
Pink arrows denote areas subject to neuromodulators.

Nitric oxide (NO), which is produced by the cardiac muscle upon contraction, is known to provide negative feedback to the CG. This NO diffused to the CG decreases the frequency of the driver potential bursts, which causes a decrease in heartbeat frequency and contraction amplitude [16, 30, 37]. Thus, previous studies have hypothesized that the level of NO present in the heart provides feedback to the CG about the degree of contractions and allows the CG to alter its activity in response [18].

The rhythmic heartbeat of the lobster is also thought to be responsive and possibly even dependent on the stretch feedback from the myocardium [2]. The array of cardiac ligaments, which suspend the heart, are stretched during systole. During diastole, the elastic recoil of the alary ligaments contribute to filling the heart with hemolymph through the ostia by a negative pressure gradient between the single ventricle of the heart and the pericardial sinus [46].

Stretch feedback from the myocardium is sent to the CG through stretch sensitive dendrites and affects the motor neurons and the pacemaker cells. Since the CG is responsible for the the heart's contraction, it determines the whole heart contraction cycle period. Therefore, previous experiments found that tonic stretch elicits a decrease in contraction cycle period in the majority of whole hearts. However, stretch increases cycle period in some lobster hearts. Therefore this stretch feedback is more complex than expected [18].

This important feedback mechanism allows the CG to sense relevant changes, such as the degree of filling in the heart, and to integrate this information to appropriately adjust motor output. For example, lobsters rapidly take up water while molting in order to push apart

their exoskeleton and expand their new soft exoskeleton. As a result of this, water uptake and resulting increase in hemolymph volume, the heart rate increases just prior to ecdysis [28, 32].

The goal of the current study was to determine the mechanism underlying stretch responsiveness. Investigating this mechanism will help gain an understanding of how the various modulatory and feedback components of a CPG-effector system are capable of producing a highly flexible stereotyped motor output.

1.4. **Possible Mechanosensitive channels involved.**

Mechanical stimuli drive many physiological processes, including touch and pain sensation, hearing, and blood pressure regulation. The process by which mechanical forces on the myocardium can change its electrical properties is termed mechanoelectric feedback. This feedback has been demonstrated in many animal models, including isolated cells, isolated hearts, and whole organisms, including humans, where it is demonstrated directly in both the atria and the ventricles. It is likely that mechanoelectric feedback provides either the trigger or the substrate for some types of clinically important arrhythmia. Mechanoelectric feedback may arise due of the presence of stretch-sensitive (or mechano-sensitive) ion channels in the cell membrane of the cardiac myocytes.

Stretch-sensitive ion channel activities have been recorded in many cells, but the responsible molecules have not been identified [4]. Additionally, stretch-activated ion channels open in response to stretch and have been identified to underlie mechanoelectric feedback processes in several invertebrate and vertebrate species [27, 13, 17, 12]. Stretch-sensitive ion channels are known to be responsible for mechanoelectric feedback processes in the abdominal stretch receptor organ in decapod crustaceans [13]. Stretch-sensitive ion channels can be nonselective cation channels or selective sodium, potassium or chloride channels [12]. It has been hypothesized that the mechanoelectric feedback in the cardiac ganglion occurs through the opening of a stretch-sensitive ion channel in motor neurons.

Stretch-Sensitive Chloride channel

One hypothesis is that stretch feedback results from the opening of stretch-sensitive chloride channels. Stretch-sensitive chloride channels have been described in several cells, such as vertebrate myocytes [17] and *murine microglia* [12], although they have not previously been described in crustaceans. Chloride channels in these other organisms have minimal permeability to chloride at rest and therefore do not contribute to the resting membrane potential in most neurons. Previous studies have examined ionic currents in the CG neurons in the crab, *Cancer borealis*, and did not report any chloride currents contributing to the pacemaker potential in these neurons, suggesting that chloride does not contribute to the pacemaker potential [38, 33, 34]. Although chloride currents in the heart of the crustacean have not previously been identified, chloride equilibrium potential is very close to the resting membrane potential in the muscles of spiny lobsters and crayfish [25, 26, 1]. Thus, if chloride were to have an equilibrium potential close to that of the membrane potential of cardiac ganglion neurons, it could explain the CGs variable responses to stretch because variations in the membrane potential from heart to heart can impact the driving force on chloride ions through these channels. When the membrane potential is more depolarized than the reversal potential of the cardiac ganglion motor neuron, there is a driving force on chloride to flow out of the cell at rest. Thus, when stretch-sensitive chloride channels open in response to stretch, the membrane potential slightly depolarizes. This would decrease the time to reach driver potential threshold and ultimately

increase heartbeat frequency. Alternatively, when the membrane potential is more hyperpolarized than the chloride reversal potential, there is a driving force on chloride to flow into the cell at rest. Thus, in this case, when chloride channels open in response to stretch, the pacemaker potential would slightly hyperpolarize and as a result, it would take longer to reach driver potential threshold. Consequently, it would take longer to reach threshold and the heartbeat frequency would decrease. Finally, when no response to stretch is observed in the semi-intact heart, it might be the case that the membrane potential is equal to that of the chloride reversal potential. At rest there would be no driving force on chloride and therefore no change in the pacemaker potential would occur.

Other Stretch-Sensitive Channels

Another hypothesis is that mechanoelectric feedback results from the opening of two types of stretch-sensitive channel, which have previously been studied: (1) a non-specific cation stretch-sensitive channel and (2) a stretch-sensitive potassium channel. The gene coding for the stretch-sensitive channel has not yet been identified [8]. Current research attempts to identify mRNAs encoding several potential mechano-gated channels in a neural transcriptome generated from the *Callinectes*' CG. These include a Piezo-2 type cation channel [4] and homologs to the TREK-1 mechano-gated K^+ channel [14]. The currents of these channels do not require cytoskeletal elements or second messengers. Using Xenopus oocytes, currents evoked these channels using a piezo-electrically driven stimulus [7, 4] (Marc W. Miller, Personal communications).

1.5. **TREK-1 mechano-gated K^+ channel.**

Background (also called baseline or leak) K^+ channels are transmembrane K^+-selective ionic pores that are constitutively open at rest and are central to neural function. The resting activity of these K^+ channels drives the membrane potential (through hyperpolarization) closer to the K^+ equilibrium potential (-80mV), and therefore tends to reduce excitability [21].

TREK-1 is a potassium background channel, which is important for setting the resting membrane potential in neuronal cells and belongs to the family of two-pore potassium (K2P) channels that are expressed in the heart [36].

Current research is underway in assigning the roles of this channel in the cardiovascular system, but difficulty arises due to the lack of specific antagonist. It has been proposed that TREK-1 may be involved in Mechanoelectric feedback regulation. It is possible that more/fewer TREK-1 channels open upon stretch, causing more K^+ current, reducing the excitability of the neuron. TREK-1 may also be involved in modulating natriuretic peptide secretion by atrial myocardium [36].

Additionally, it is important to note that Honore (2006) demonstrated that TREK-1 shows pronounced desensitization, similar to native stretch-sensitive K^+-channels. Kinetic models show that desensitization can be accounted for without introducing adaptation of the stimulus. Additionally, Honore envisions that the activation involves a torque; specifically it is envisioned that the channel opens asymmetrically in the outer and inner monolayers generating a torque about some point within the membrane interior. Typically, the current of the channel peaked in 20 ms and desensitized over 100 ms. The desensitization was monoexponential with a time constant of 46 ms at 1650 Pa [11].

1.6. **Piezo 2-type cation channel.**

Piezo homologues are found in organisms as diverse as plants, protozoa, and invertebrates. Phylogenetic analyses suggest that in vertebrates, Piezo-1 diverged from Piezo-2, as most lower organisms carry a single Piezo protein, whereas vertebrates have two. The exception is pathogenic protozoa, where homologues of Piezo are present in two groups genetically distinct from mammalian Piezo-1 and Piezo-2. Multispecies sequence alignments of evolutionarily distant protozoa, amoeba, plant, insect, and vertebrate Piezos reveal a remarkably conserved motif, the PFEW domain, hypothesized to be involved in channel conductance or gating [5].

Mechanically-activated currents through the Piezo-like channels are characterized by a linear current-voltage relationship with a reversal potential around 0-10 mV, consistent with it mediating a non-selective cationic conductance [7].

2. Experimental Methods

2.1. **Lobsters.**

Experiments were performed by many current and previous members of the Dickinson Lab at Bowdoin College, including E.S. Dickinson, K. Harmon, X. Qu, and K. Suchyta.

Both sexes of lobsters (0.5-0.9kg) were purchased from local (Brunswick, Maine) fish markets and housed in recirculating natural seawater aquaria at 10-12°C. Lobsters were fed weekly and maintained on a 12:12 dark light cycle. All experiments were performed in chilled (8-12°C) physiological saline (composition: 479.12mM NaCl, 12.74 mM KCl, 13.67 mM CaCl2, 20.00 mM MgSO4, 3.91 mM Na2SO4, 11.45 mM Trizma base, 4.82 mM maleic acid [pH 7.45]).

2.2. **Dissection.**

Lobsters were removed from the aquarium and were anesthetized on ice for 30 minutes. Then, the tail, walking legs, and claws were removed and incisions were made along the posterior dorsal side of the thoracic carapace on both sides of the heart. The arteries and elastic ligaments were cut to remove the intact heart attached to the carapace. The heart was then scraped away from the carapace and pinned ventral side up in a small Sylgard (KR Anderson, Santa Clara, CA, USA)-lined dish filled with chilled saline. To expose the cardiac ganglion, the ventral wall of the heart was cut longitudinally toward the lower posterior artery.

A bundle of muscles underlying and surrounding the posterior end of the cardiac ganglion (which contain the premotor neurons) were isolated, as shown in **Figure 4**, below. GLUture topical tissue adhesive (Abbott Laboratories, North Chicago, IL, USA) was applied using the tip of a small glass probe to prevent the bundle of muscle fibers from falling apart following dissection from the heart. Chilled saline was poured back on the heart once the tissue adhesive was dry.

2.3. **Electrophysiological recordings.**

A windows computer with Spike2 version 7.14 (Cambridge Electronic Design, Cambridge, UK) computer software was used for recordings. The sheath above the large motor neuron to be recorded from was removed. Glass microelectrodes (Resistance: 20-50MΩ) filled with squid cytoplamic fill (composition:20mM NacL, 15mM Na_2SO_4, 10mM Hepes, 400mM Potassium gluconate, and 10mM $MgCl_2$, Scott Hooper et al. 2015) recorded the activity from the somata

of the motor neuron. These recordings were amplified with an AxoClamp 2B amplifier (Axon Instruments) equipped with a 0.1X head stage. A petroleum jelly well was built around one of the anterolateral motor nerves. Using stainless steel wire electrodes, which were placed into the well, extracellular activity was recorded with a differential AC amplifier (A-M Systems). Intra- and extra-cellular activity was further amplified with a Model 210A Brownlee Precision Instrumentation amplifier with a 3Hz filter and digitized using a CED Micro 1401 data acquisition board.

Dynamax Peristaltic pump (Rainin, model RP-1) superfused chilled saline over the preparation using at a rate of 5mL/minute. The temperature was maintained at 8-12°C in all preparations using a Peltier temperature control system (CL-100 bipolar temperature controller and SC-20 heater/cooler; Warner Instruments, Hamden, Connecticut, USA).

2.4. **Computer Modulated Stretches.**

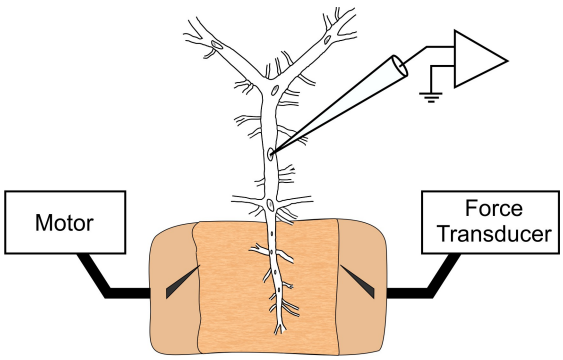

FIGURE 4. Diagram of setup for stretch experiments.

The isolated bundle of cardiac muscle was attached with a SI-TM2 pointed hook tissue mount (World Precision Instruments, Sarasota, FL, USA) to a SI-KG4 optical force transducer (World Precision Instruments, Sarasota, FL, USA) controlled by a micromanipulator. The other end of the muscle bundle was attached with a SI-TM2 pointed hook tissue mount to a SI-H linear motor (World Precision Instruments, Sarasota, FL, USA) as shown by **Figure 4**, above. The glued ends of the muscle aided in securing the muscle bundle to the hook tissue mounts. The muscle bundle was stretched linearly in a ramp. Stretches ranging from 0.5-1.2mm were applied to the muscle for five seconds, with varying rates of stretch and release (strain rate) across all stretches.

A linear motor controller (SI-MOTDB, WPI) was used to control the movement of the motor based on stretch output commands programmed using Spike2 multi-channel continuous data acquisition and analysis package. The force applied to the cardiac muscle during stretch was measured with SI-KG4 optical force transducer and amplified with amplified with a BAM21-LCB amplifier (World Precision Instruments, Sarasota, FL, USA) and digitized using Spike2. A CED Micro 1401 data acquisition board was used to record the force output of the PC using Spike2 V7.03.

2.5. **Current Injection.**

To determine whether stretch of the myocardium causes the opening of stretch- activated channels, pulses of hyperpolarizing and depolarizing currents can be injected into the cell during stretch to observe changes in the membrane resistance.

Lobsters were first dissected and electrophysiological recordings were performed per protocol as explained above. In addition to the glass microelectrode to recorded the activity from the somata of the motor neuron, a second glass microelectrode was used to inject computer modulated current into a different motor neuron of the same CG.

2.6. **Ligation.**

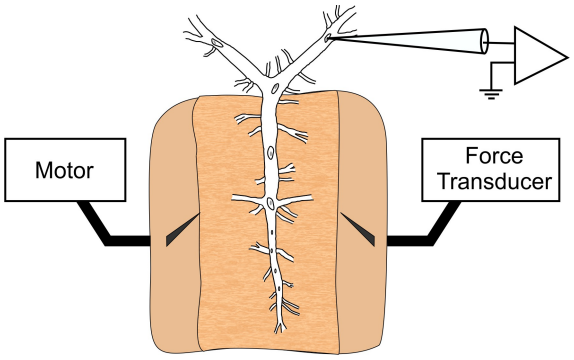

FIGURE 5. Diagram of experimental setup before ligation

Lobsters were first dissected per protocol as explained above. However, for the ligation experiments, the muscles surrounding the entire main trunk of the CG were isolated and GLUture kept them intact. The hooks for the computer modulated stretches were placed in middle of trunk's muscle and the entire muscle moved when stretch was applied as shown in **Figure 5**, above. Electrophysiosological recordings and computer modulated stretches were then performed per protocol as explained above. Both the small and large cells were stretched and the recordings included signals from both the small and large cells.

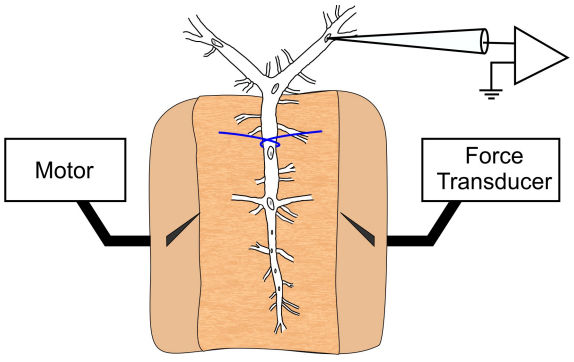

FIGURE 6. Experimental Setup after ligation. (Blue tie around CG denotes the suture silk used for ligation.)

Following these initial stretch experiments, one thread of the suture silk was tied around the trunk, close to cell 4 to block the signals from the small cells, as shown in **Figure 6**, above. After ligation, the CG neurons stabilized, and the stretch experiments were repeated. **Figure 7**,

below, diagrams the schematic overview of the CG, depicting that before ligation, information from axon of premotor neurons travels up axons to the motor neurons, however, after ligation, this information is prevented from reaching the motor neurons. Thus, after ligation, although stretching both the small and large cells, the recordings only included signals from the large cells.

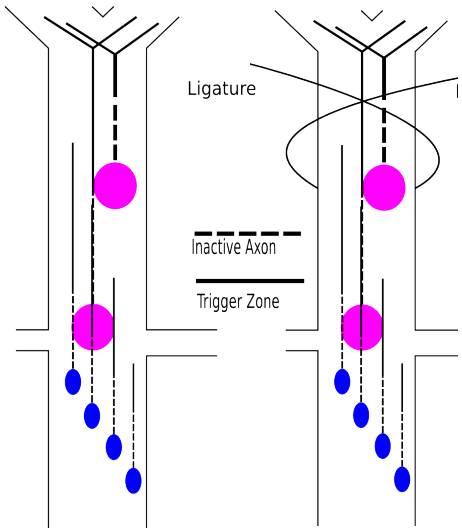

FIGURE 7. Schematic overview of CG before (left) and after (right) ligation. Pink dots represent the motor neurons and the blue cells denote the pacemaker neurons. (From A.L. Martimer, 2012).

2.7. **Data analysis.**

Raw data were analyzed using in house written scripts for Spike2 that measured the driver potential amplitude, frequency, burst duration, number of spikes per burst, and duty cycle. The data used for analyses were organized, graphed, and analyzed in Prism and Excel using house written scripts by E.S. Dickinson.

3. Experimental Results

3.1. **Response of CG neurons to stretch consists of three separate components.**

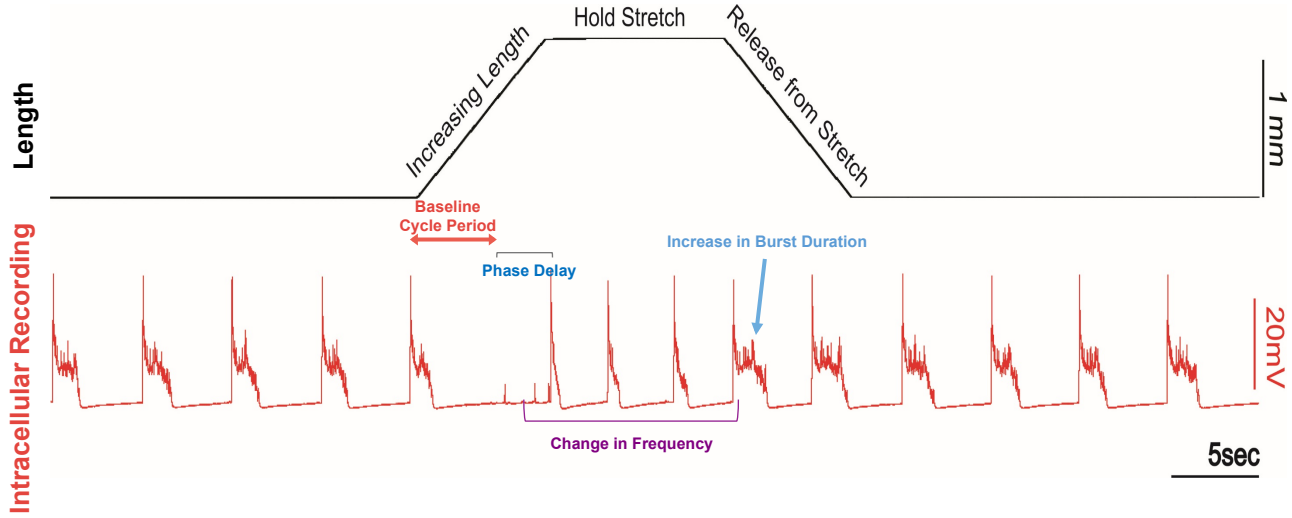

Figure 8. Example intracellular recording of a motor neuron during a stretch experiment. Recording depicts the three characteristic components of the CG's stretch response: phase delay, frequency change, and increase in burst duration.

Component 1: Phase Delay

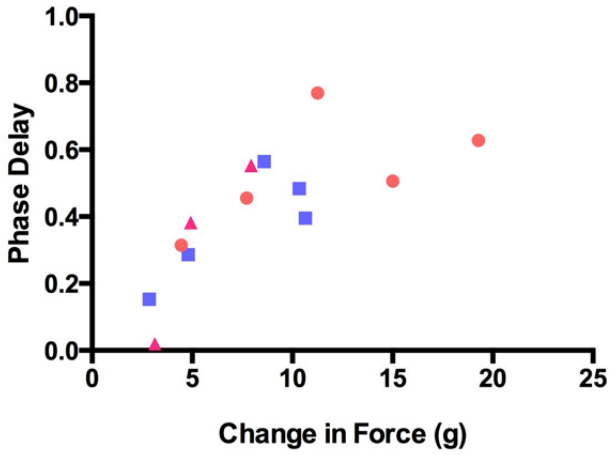

Figure 9. During the up ramp of stretch, the CG exhibited a delay in the burst of the subsequent driver potential, i.e., a phase delay. The phase delays increased as a function of the force due to stretch. Pooled data from 3 lobsters. Each symbol represents a lobster.

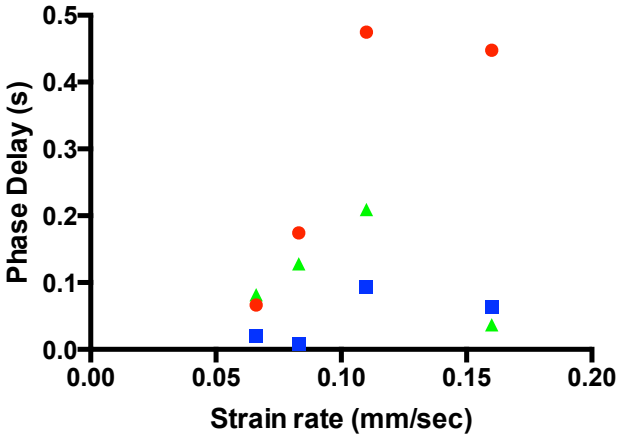

FIGURE 10. Additionally, the phase delay increases as a function of strain rate of stretch. The delay in the burst of the next driver potential increased with increasing rate of stretch (strain rate) for strain rates less than 0.15 mm/sec. Pooled data from 3 lobsters. Each symbol represents a lobster.

Component 2: Change in frequency

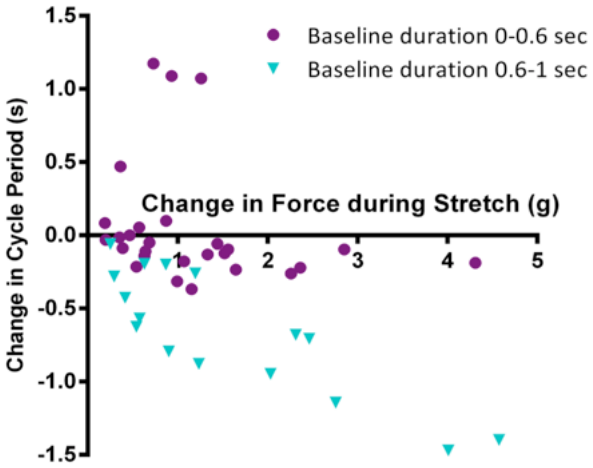

FIGURE 11. The response of the CG neurons to stretch depends on both stretch amplitude and baseline characteristics of CG neuron bursts. The cycle period decreased (frequency increased) as a function of stretch magnitude (force), but only in motor neurons with long initial driver potential durations (>0.6sec). Pooled data from 19 lobsters.

Component 3: Increase burst duration

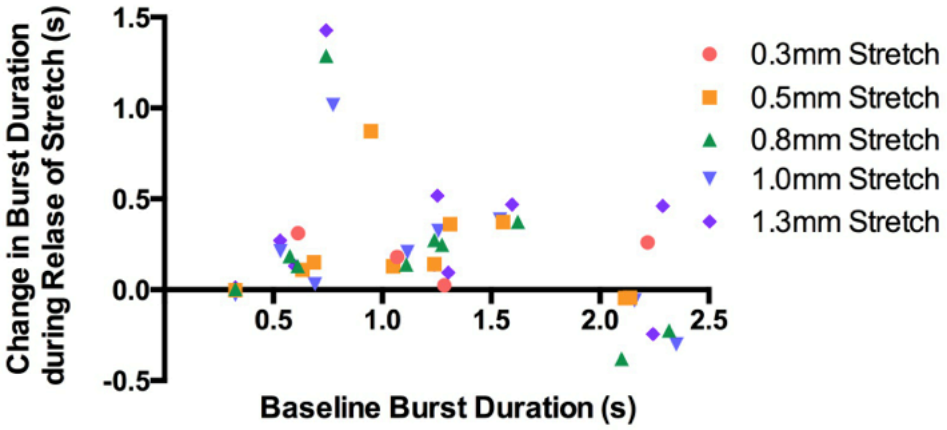

FIGURE 12. Upon return from stretch, the CG exhibited an increase in the burst duration of the driver potential. However, this trend is only apparent in motor neurons with relatively long bursts (>0.6s). Among these neurons, burst duration decreased with increasing initial burst duration. Driver potential duration did not increase during release from stretch in motor neurons with the shortest initial bursts (<0.6s).

3.2. **Current Injection.**

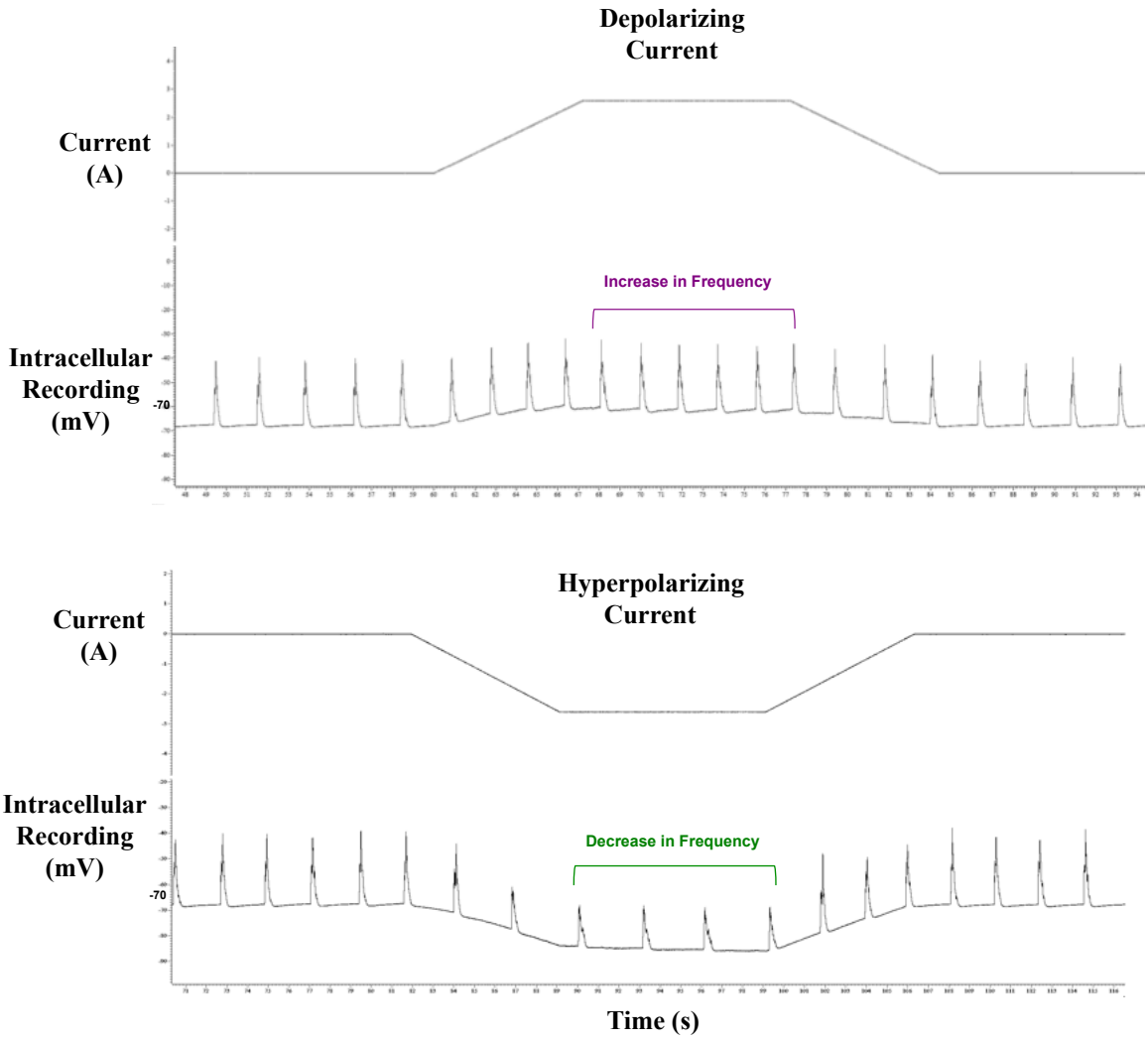

FIGURE 13. Example intracellular recordings of a motor neuron during current injection experiments. Recording depicts the typical response of the CG to depolarizing (top) and hyperpolarizing (bottom) current injections.

Preliminary data suggests that injection of depolarizing current caused an increase in frequency, while injection of hyperpolarizing current caused a decrease in frequency, similar to the characteristics of component two of the stretch response. None of the current injection protocols mimicked all three components of the CG's response to stretch. Current injections are instantaneous, constant, and have a single reversal potential. Although we can change the characteristics of the current (hyperpolarizing versus depolarizing currents) to see different responses, these data suggest that the feedback from stretch is not mediated by the opening of a single stretch-sensitive ion channel.

3.3. **Ligature.**

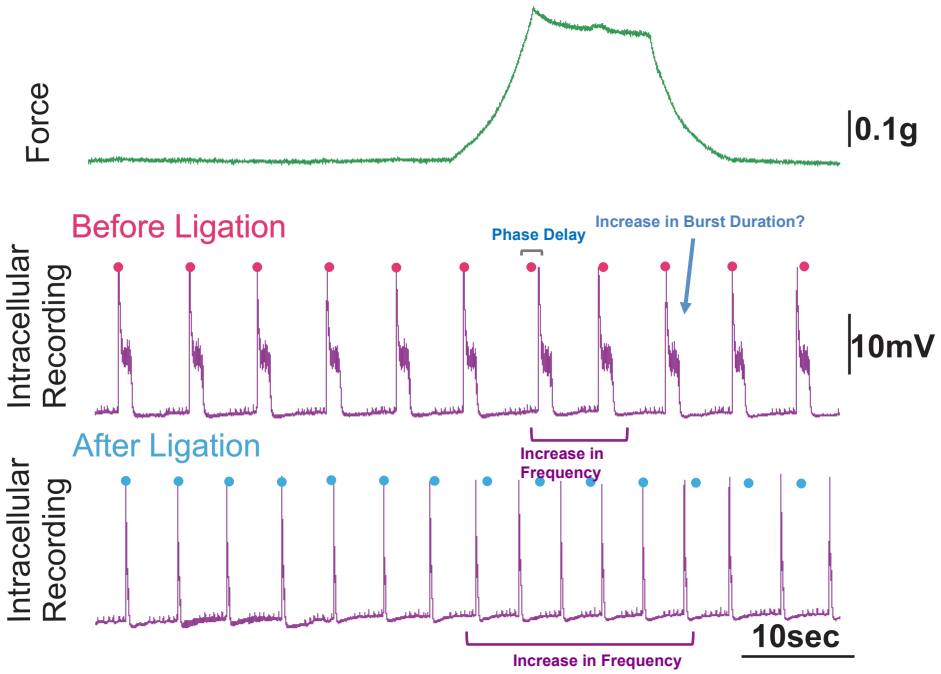

FIGURE 14. Example intracellular recordings of a motor neuron during stretch experiments before and after ligation. The recordings depict the typical responses of the CG to stretch before ligation (top) and after ligation (bottom). The dots above each recording indicate the intrinsic driver potential period of the CG's motor neuron.

As shown by the preliminary data shown above (**Figure 14**), an increase in frequency during stretch is observed before and after ligation. Thus, upon stretching large and small cells, but blocking the electrical and chemical signal from small cells, stretch still causes the motor neurons to increase frequency (**Component 2**). Therefore, we hypothesize that both cell types have stretch-sensitive ion channels causing the cycle period to change.

Before ligation, the small cells and the large cells are still chemically and electrically coupled and the muscle underlying and surrounding the trunk of the CG intact, the CG's phase delay during the increasing length of stretch (**Component 1**) is apparent. Additionally, the CG's driver potential increase in burst duration during release from stretch (**Component 3**) is questionably present. More data is required for further analysis. Upon ligation, when the electrical and chemical coupling between the two cell types is lost, both **Component 1** and **Component 3** of the stretch response are lost after ligation.

There are two possible explanations for these results. First, we could hypothesize that the first component of the stretch response is due to the input stretch has on the small pacemaker cells only (possibly stretch sensitive channels that are only present on the small cells). Thus, the loss of the the phase delay is due to the loss of the stretch input into the small cells when ligated. An alternative explanation is the loss of these stretch response currents is due to the interactions between the large and small cells. Thus, the loss of the driver potential phase delay and increase in burst duration are due to the loss of the small and large cell electrical and chemical interactions upon ligation.

Part 2. Computational

4. Introduction

4.1. Mathematical Model Description.

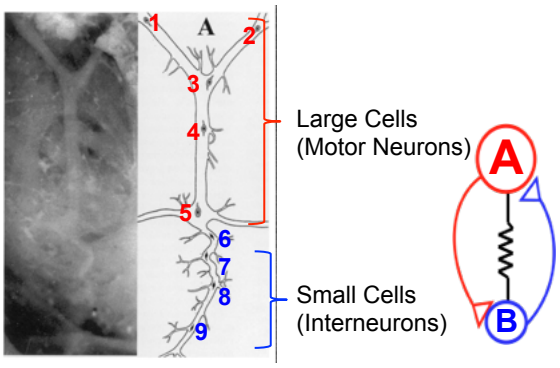

Figure 15. Two oscillating cell types: Large Cells (A) and Small Cells (B).

Modeling studies have examined the behaviors of synchronous networks, specifically in terms of cycle frequency and phase relationships and maintenance. Although the CG consists of nine neurons, each individual large cell and small cell has nearly identical electrical properties to its respective group. Therefore, each group can be modeled as a single oscillator, denoted by A and B in **Figure 16** [22, 23, 39, 38, 15, 42].

One way to exploit the similarity between the cells to approach the dynamic interactions among the large cells and small cells is to explore the interaction of the two oscillators. Williams et al. (2013) built a conceptual two-cell model of the CG using a pair of Morris-Lecar oscillating neurons coupled by an electrical synapse and reciprocal excitatory chemical synapses (Figure 15). Each model neuron consists of a fast, non-inactivating Ca^{2+} current and a slow, non-inactivating K^{+} current, representing the inward calcium currents and outward voltage and calcium-dependent potassium currents, respectively, which drive the slow-wave oscillating driver potentials and their action potentials, as explained in Section 2.2. In addition, a depolarizing leak current was added to each model neuron with a reversal potential at $-10mV$ to represent the hypothesized depolarizing pacemaker potential due to sodium currents, which initially activate the driver potentials.

Single Morris-Lecar Model Cell
The equations governing a single Morris-Lecar model are:

$$C\frac{dV}{dt} = -g_L(V - V_L) - g_{Ca}M_\infty(V - V_{Ca}) - g_K W(V - V_K) \tag{1}$$

$$\frac{dW}{dt} = \lambda_W(W_\infty(V) - W)$$
$$\lambda_W = \phi_W \cosh\left[\frac{1}{2}\left(\frac{V - V_3}{V_4}\right)\right]$$
$$M_\infty = \frac{1}{2}\left[1 + \tanh\left(\frac{V - V_1}{V_2}\right)\right]$$
$$W_\infty = \frac{1}{2}\left[1 + \tanh\left(\frac{V - V_3}{V_4}\right)\right].$$

The variable V denotes the membrane potential of the model neuron and the variable W denotes the proportion of open K^+ channels. The parameter C denotes the capacitance of the model neuron, g_L, g_{Ca}, and g_k are the leak, Ca^{2+}, K^+ conductances, respectively; and V_L, V_{Ca}, and V_K are the leak, Ca^{2+}, K^+ reverse potentials. The function M_∞ represents the proportion of open Ca^{2+} channels at steady state, which are assumed to open instantaneously. The function W_∞ represents the proportion of open K^+ channels at steady state. The K^+ channels are not assumed to open instantaneously. Instead, their opening is governed by the differential equation for $\frac{dW}{dt}$ with time constant λ_W as a function of V. The parameter ϕ_W represents the minimum value of λ_W over all V. Finally, V_1 and V_3 are the half-activation values for the Ca^{2+}, and K^+ currents, and V_2 and V_4 control the slope of the the Ca^{2+}, and K^+ currents at the point of half-activation.

Two Coupled Morris-Lecar Model Cells

The equations governing the dynamics of a two-cell system with electrical and chemical coupling are:

$$(2)\quad C\frac{dV^A}{dt} = -g_L^A(V^A - V_L) - g_{Ca}^A M_\infty(V^A - V_{Ca}) - g_K^A W(V^A - V_K) - g_{Syn}^A S_\infty(V^B)(V^A - V_{Syn}) - g_{gap}(V^A - V^B)$$

$$\frac{dW^A}{dt} = \lambda_W(W_\infty(V) - W^A)$$

$$(3)\quad C\frac{dV^B}{dt} = -g_L^B(V^B - V_L) - g_{Ca}^B M_\infty(V^B - V_{Ca}) - g_K^B W(V^B - V_K) - g_{Syn}^B S_\infty(V^A)(V^B - V_{Syn}) - g_{gap}(V^B - V^A)$$

$$\frac{dW^B}{dt} = \lambda_W(W_\infty(V) - W^B)$$
$$\lambda_W = \phi_W \cosh\left[\frac{1}{2}\left(\frac{V - V_3}{V_4}\right)\right]$$
$$M_\infty = \frac{1}{2}\left[1 + \tanh\left(\frac{V - V_1}{V_2}\right)\right]$$
$$W_\infty = \frac{1}{2}\left[1 + \tanh\left(\frac{V - V_3}{V_4}\right)\right]$$
$$S_\infty(V^{pre}) = \frac{1}{2}\left[1 + \tanh\left(\frac{V^{pre} - V_5}{V_6}\right)\right].$$

Where g_{Syn} and g_{gap} represent the chemical synaptic, and electrical synaptic maximal conductances respectively and V_{syn} is the reversal potential of the chemical synaptic current. In the additional sigmoidal function S_∞, governing the chemical synaptic conductance, the presynaptic potential V^{pre} for cell A is V^B and vice versa.

The function, S_∞ denotes the proportion of open chemical synaptic channels at steady state, which are assumed to open instantaneously. Additionally, the parameter V_5 represents the half-activation value for the chemical synaptic current and V_6 controls the slope of the chemical synaptic current at the point of half-activation.

For all simulations, the following variables were kept constant: $C = 10$ nF, $V_L = -10$ mV, $V_{Ca} = 100$ mV, $V_K = -80$ mV, $V_1 = 0$mV, $V_2 = 15$ mV, $V_3 = 0$ mV, $V_4 = 15$ mV, $V_5 = 0$ mV, $V_6 = 5$ mV, and $\phi_W = 0.002$ msec.

Note: This coupled Morris-Lecar model includes the medium speed noninactivating Ca^{2+}-current, a slow noninactivating K^+-current, and a leak current, but not a fast sodium current. The currents included are those assumed to be responsible for producing the slow driver potential oscillations in the membrane potentials. Therefore, this model does not attempt to capture the fast dynamics of the action potentials with individual bursts, but instead captures the slow dynamics of the driver potentials underlying the bursts within the neurons. Thus, the model neuron is considered to be bursting whenever the membrane potential depolarizes above 0 mV [47].

Williams et al. (2013) simulated 15,000 model networks by randomizing the conductance parameters of the neurons. Among these simulations, 13,141 networks produced synchronous oscillations, which varied in terms of frequency and cell phasing, similar to the natural variability seen in experimental data. Thus, this study showed that the synchronous oscillation patterns of the CG, which vary in terms of cycle frequency and phasing, matched a pattern found in the modeled parameter space, confirming that this region of parameter space reflects that of the actual biological system. Throughout this report, we use a model example from the physiologically meaningful region of parameter space identified by Williams et all. (2013) [47].

Morris-Lecar equations are extensively used in the mathematical biology literature. Through further exploration of coupled Morris-Lecar oscillators, one of our goals is to show that these equations can facilitate more rigorous and complete understanding of the model CG network. XPP and MatLab R2015a programs were used for all numerical simulations. The conclusions that result may then be generalizable to other model and biological networks [40, 29].

In this report, we propose ways of gaining understanding of how the CG intrinsic excitability, motor pattern, and coupling causes the network to respond to stretch perturbations. Specifically, we attempt to reproduce the three complex components of the CG neurons's stretch response, observed experimentally, to gain a better understanding of the mechanism behind the CG's stretch feedback.

5. Single Decoupled System

5.1. **Introduction.**

For the computational part of this project, we begin by looking at a two-dimensional system of a single decoupled Morris-Lecar oscillator, which models the behavior of either the small cells or the large cells. We first chose to look at the large cells in isolation, since these are the cells we are able to record from experimentally. **Equations 1-5**, above, govern the Morris-Lecar dynamics of the large cells in isolation. In Section 11, we return to the fully coupled system of two cells, to see the impact of the environment (i.e., feedback mechanisms and interactions with the small cells) on the large cells.

5.2. **Model Response to Current: Methods.**

By decoupling the original two-cell system, we have removed the electrical and chemical coupling as well as the Morris-Lecar dynamics of the small cells to remove the influence of other cells. However, similar to experimental methods of injecting hyperpolarizing and depolarizing currents to determine whether stretch of the myocardium causes the opening of stretch-activated channels, we can introduce an applied current into the decoupled model. Thus, to look at the possible effects of stretch through stretch sensitive ion channels in the decoupled large cells, we incorporated an applied current I_s :

$$C\frac{dV}{dt} = -g_L(V - V_L) - g_{Ca}M_\infty(V - V_{Ca}) - g_K W(V - V_K) + I_s \tag{4}$$

$$\begin{aligned}
\frac{dW}{dt} &= \lambda_W(W_\infty(V) - W) \\
\lambda_W &= \phi_W \cosh\left[\frac{1}{2}\left(\frac{V - V_3}{V_4}\right)\right] \\
M_\infty &= \frac{1}{2}\left[1 + \tanh\left(\frac{V - V_1}{V_2}\right)\right] \\
W_\infty &= \frac{1}{2}\left[1 + \tanh\left(\frac{V - V_3}{V_4}\right)\right].
\end{aligned}$$

By varying the applied current I_s, this model will show the possible effects of hyperpolarizing and depolarizing current on this single cell type.

Example 1

Let's take, for example, one parameter set from the physiologically meaningful region of parameter space identified by Williams et al. (2013) for a two-cell-type model, decouple the cells, and investigate the effects of current on the single decoupled large cell model [47]:

Single Decoupled System with I_s					
Parameter	Variable	Value Used			
Cell surface area, cm^2		0.001			
Total cell capacitance, nF	C	10			
Ca^{2+} reversal potential, mV	V_{Ca}	100			
K^+ reversal potential, mV	V_K	-80			
Leak reversal potential, mV	V_L	-10			
Ca^{2+} half activation slope, mV	V_1	0			
Ca^{2+} current activation slope, mV	V_2	15			
K^+ half activation slope, mV	V_3	0			
K^+ current activation slope, mV	V_4	15			
K^+ current minimum rate constant, ms	ϕ_W	0.002			
Ca^{2+} current maximal conductance, $\mu S/cm^2$	g_{Ca}	24			
K^+ current maximal conductance, $\mu S/cm^2$	g_K	64			
Ca^{2+} current maximal conductance, $\mu S/cm^2$	g_L	1			
Parameter	Variable	Min.	Value Used	Max.	Value Used
Stretch Current, nA	I_s	-35		100	

5.3. **Model Response to Current in the Voltage Traces: Results.**

Recall that the model represents the slow driver potential of the neurons underlying the bursts, not the fast bursting potential itself. So each action potential in the model corresponds to a burst in the data, and firing frequency in the model corresponds to burst frequency in the data, etc. Figures 16-19 depict the large cell voltage traces from Example 1 affected by the current I_s.

Depolarizing Current ($I_s > 0$nA)

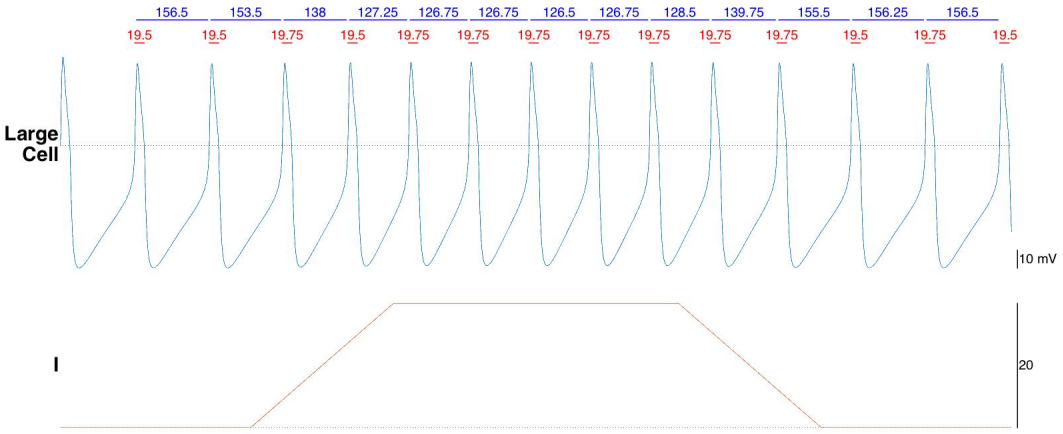

FIGURE 16. Voltage and current traces of Example 1 with $I_s = 20$nA. The x-axis is a unitless time axis showing the same time scale in all figures. The blue numbers above the voltage trace correspond to the cycle period duration of each driver potential and the red numbers correspond to the burst durations. This depolarizing current causes an increase in the rhythmic frequency of the driver potential bursts. This increase in frequency is less drastic than that in Figure 16.

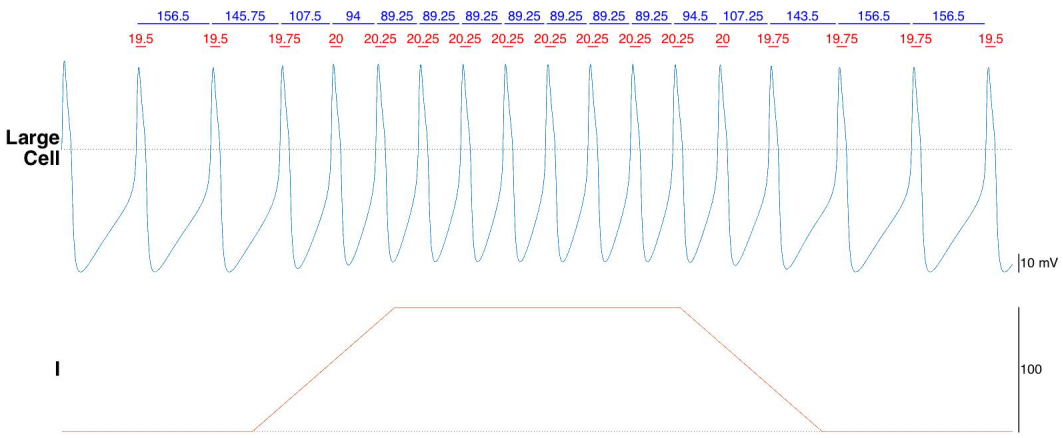

FIGURE 17. Voltage and current traces of Example 1 with $I_s = 100$nA. The x-axis is a unitless time axis showing the same time scale in all figures. The blue numbers above the voltage trace correspond to the cycle period duration of each driver potential and the red numbers correspond to the burst durations. This depolarizing current causes a drastic increase in the rhythmic frequency of the driver potential bursts.

Hyperpolarizing Current ($I_s < 0$nA)

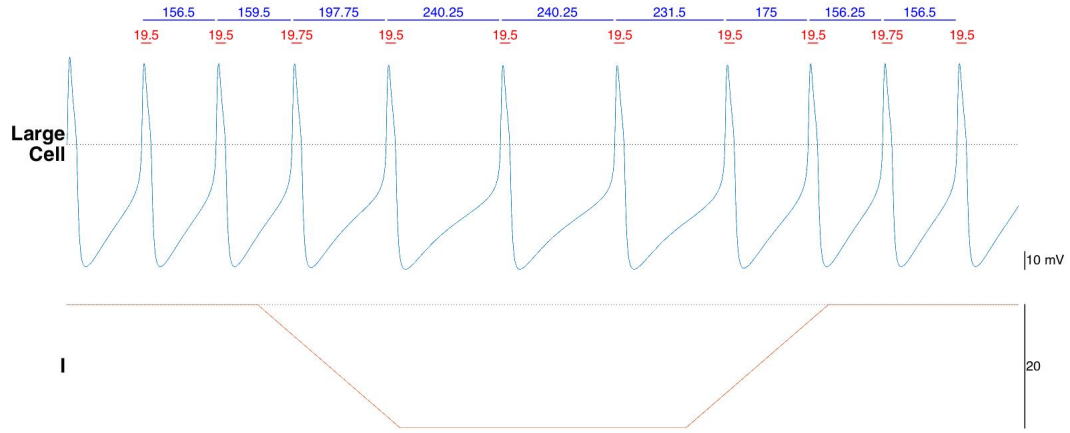

FIGURE 18. Voltage and current traces of Example 1 with $I_s = -20$nA. The x-axis is a unitless time axis showing the same time scale in all figures. The blue numbers above the voltage trace correspond to the cycle period duration of each driver potential and the red numbers correspond to the burst durations. This hyperpolarizing current causes a decrease in the frequency of the rhythmic firing pattern.

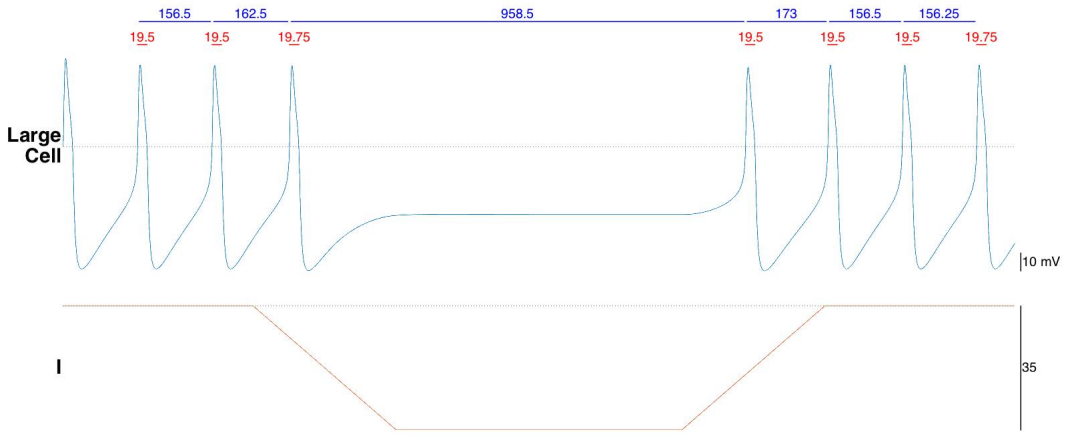

FIGURE 19. Voltage and current traces of Example 1 with $I_s = -35$nA. The x-axis is a unitless time axis showing the same time scale in all figures. The blue numbers above the voltage trace correspond to the cycle period duration of each driver potential and the red numbers correspond to the burst durations. When the hyperpolarizing current becomes too large, the model fails to cause rhythmic bursting. Throughout the duration of this current injection, the voltage trace flat-lines at the resting membrane potential, the equilibrium point of the system.

5.4. **Model Response to Current in the Voltage Traces: Conclusion.**

Summarizing, injecting hyper- and depolarizing currents into the single cell model system contributes to an observed decreased and increased frequency, respectively, which we categorize as **component 2** of the stretch response. Therefore, since this model reproduces similar results found in lab, although this is a single cell system, this confirms the usability for further manipulations and analyses to understand the model network.

Additionally, these results support the experimental data, which suggests that the feedback from stretch is not mediated by the opening of a simple stretch-sensitive ion channel since no single simple current injection led to all stretch response components. This leads us to hypothesize that multiple, complex, and possibly desensitizing mechanosensitive channels might be involved.

Although in this example, the current injection changes the frequency of the burst, only the interburst duration increases or decreases and, in fact, the burst duration during the current injection remains the same as the baseline burst duration. This also suggests that stretch is not mediated by the opening of a simple stretch-sensitive ion channel.

5.5. **Action Potential Phase Plane.**

The two dependent variables voltage (V) and K^+-channel activation (W) of the single Morris-Lecar can be plotted against each other over time. The graphical analysis of their phase plane (figures 20-24 in Section 5.6) provides information about the behavior of the model, through geometric analysis. There is no time axis in the phase plane. Instead, the progression of

time is captured by progression around the trajectory. During the rapid depolarization and hyperpolarization segments of the action potential in the voltage trace, V is changing much faster than W. This causes rapid trajectories -the horizontal segments- in the phase plane. Then, after hyperpolarization, the voltage changes more slowly, so the K^+-channels have time to close, hence a vertical segment of the phase plane. As voltage gradually returns to rest, W also stabilizes, and the trajectory approaches an equilibrium point in the phase plane. The excitability of the action potential corresponds to a large counter clockwise excursion around the phase plane before returning to equilibrium.

These phase planes can provide information for the full range of responses the cell can exhibit. Additionally, the trajectories may flow toward each other, but will never cross because of the uniqueness of solutions of ordinary differential equations. Thus, each trajectory imposes a spatial barrier to the others, which traps them in specific regions of the phase plane.

The red nullcline marks the points where $\frac{dV}{dt} = 0$ and is called the V-nullcline. It marks the points in the phase plane where the voltage turns. Biologically, this corresponds to the peaks and troughs of the corresponding voltage traces.

The green nullcline marks the points where $\frac{dW}{dt} = 0$ and is analogously defined as the W-nullcline. The nullcline marks the points where the trajectories turn from increasing W (K^+-channels opening) to decreasing W (K^+-channels closing) or vise versa.

The equilibrium is defined as a fixed point of the system where both $\frac{dV}{dt} = 0$ and $\frac{dW}{dt} = 0$. Thus, there is no change in V or W. Every intersection of the two nullclines yields an equilibrium, and every equilibrium lies at an intersection of the nullclines.

The stability of the equilibrium points is classified according to the behavior of the system near these points. If nearby initial conditions are all attracted to an equilibrium, it's stable. If they are generally repelled from the equilibrium, it's unstable. The stability can also be determined from the system of differential equations by calculating the eigenvalues of the Jacobian at the equilibrium. Stable equilibria are observable in nature and experimentally, while unstable equilibria are much more difficult to observe.

We can now translate between the traditional time courses and the phase plane. Each action potential in the voltage trace corresponds to an excursion around the phase plane. The resting potential corresponds to an equilibrium. When trajectories converge to a point where $\frac{dV}{dt} = 0$ and $\frac{dW}{dt} = 0$, an equilibrium point arises and the bursting flat-lines at the resting potential.

The phase plane helps to gain an understanding of the behavior of the decoupled single cell. The time courses of the voltage trace show the detailed response to a given stimulus/initial condition. The phase plane shows the qualitative response to all initial conditions at once, indicating how the firing pattern is generated from the differential equations, how the nullclines locate equilibria, and how the pattern of behavior is organized.

5.6. **Model Response to Current in the phase portrait: Results.**

The single cell has two independent variables. Thus, to gain an understanding of the single cell behavior, we can build a phase plane, which indicates how the pattern of behavior is organized. Figures 20-24 depict the phase portraits of Example 1 with $I_S = 0, 20, 100, -20$ and -35nA.

No Current ($I_s = 0$nA)

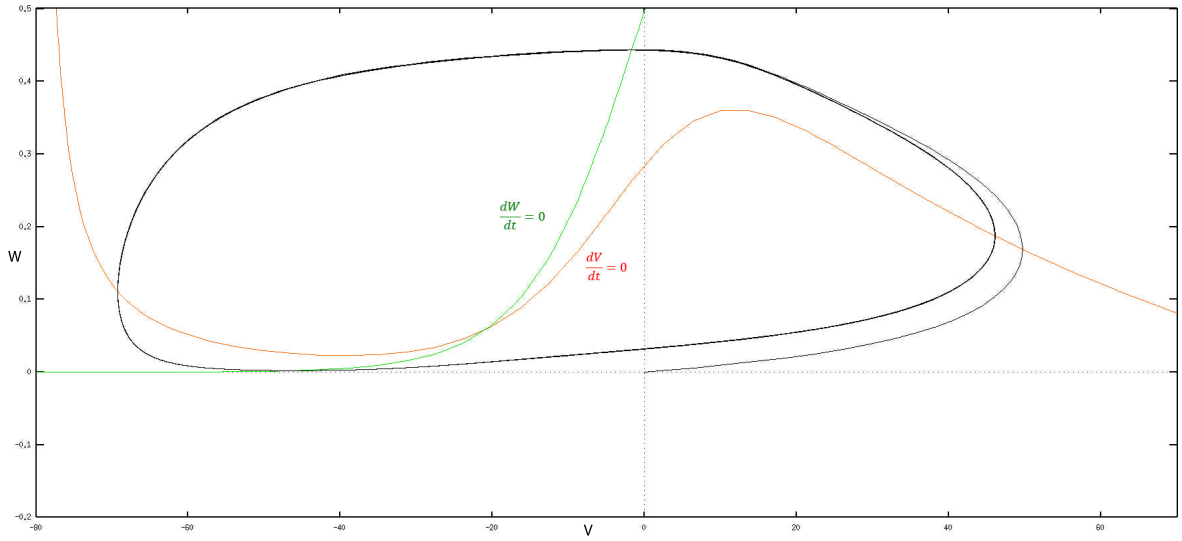

FIGURE 20. Phase portrait of Example 1 with $I_s = 0$nA.

Depolarizing Current ($I_s > 0$nA)

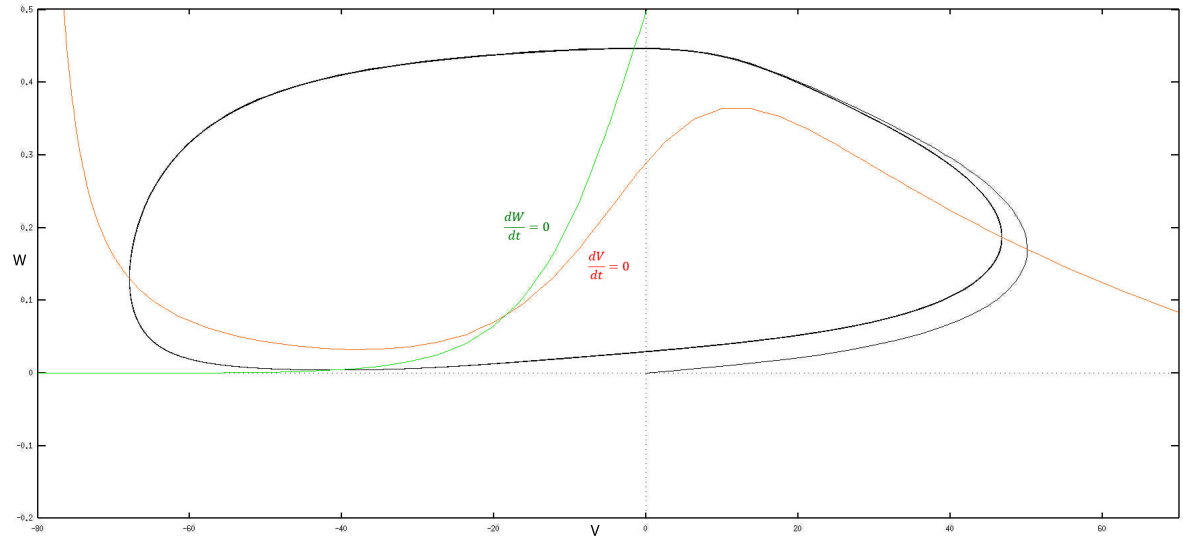

FIGURE 21. Phase portrait of Example 1 with $I_s = 20$nA.

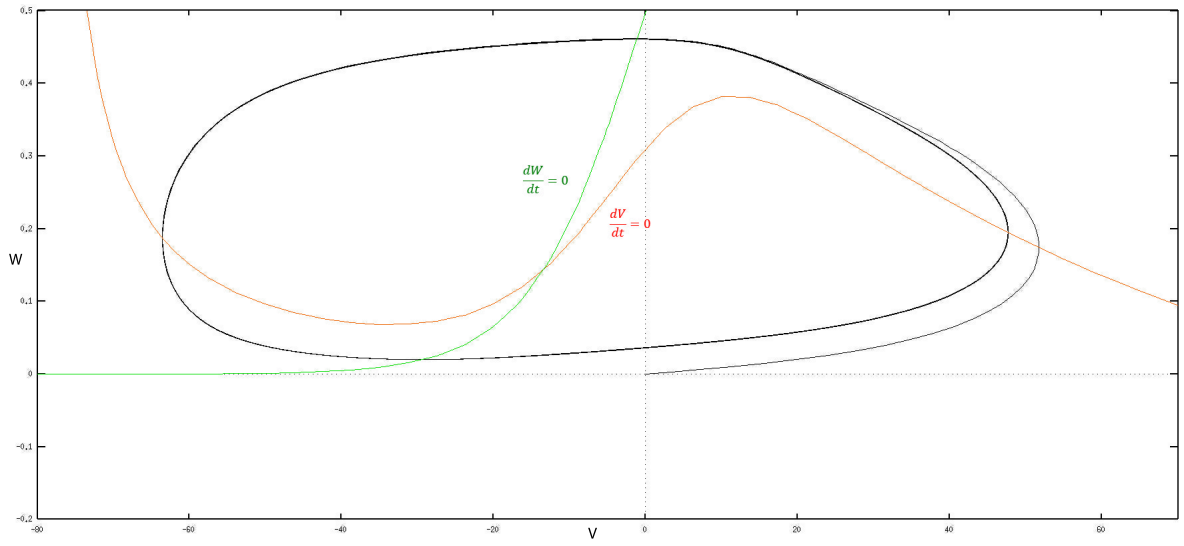

FIGURE 22. Phase portrait of Example 1 with $I_s = 100$nA.

Hyperpolarizing Current ($I_s < 0$nA)

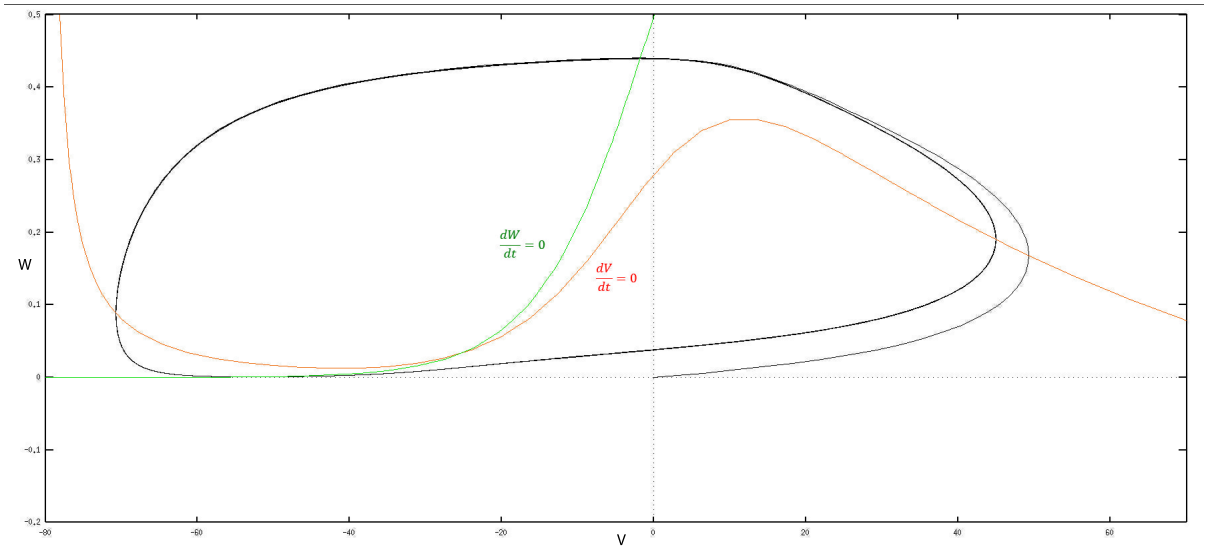

FIGURE 23. Phase portrait of Example 1 with $I_s = -20$nA.

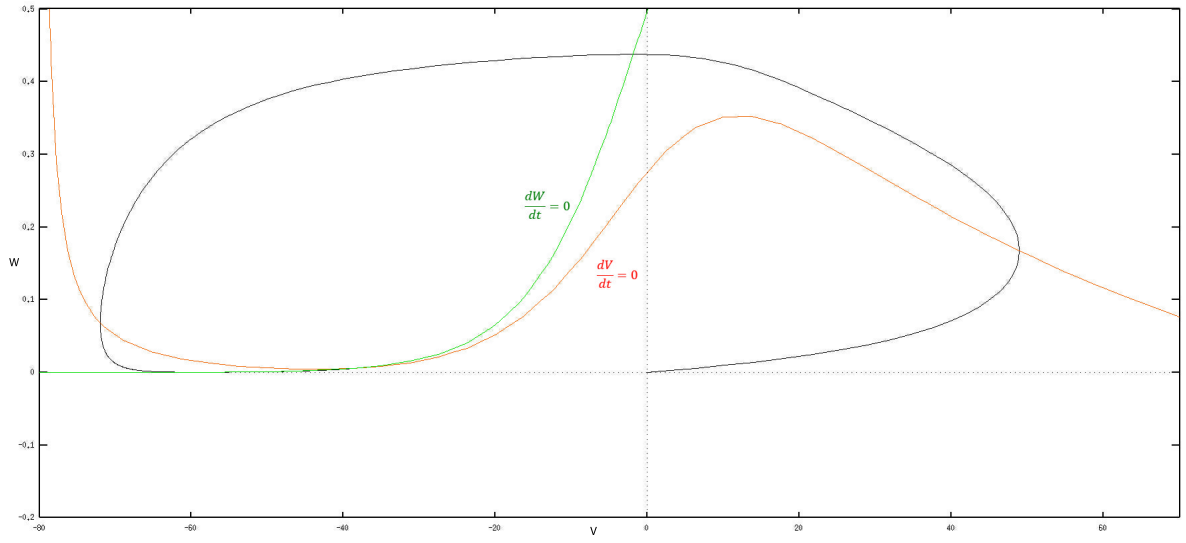

FIGURE 24. Phase portrait of Example 1 with $I_s = -35$nA.

5.7. **Model Response to Current in the phase portrait: Conclusion.**

The depolarizing current ($I_s > 0$ nA) causes the red nullcline to move up, pulling the equilibrium point (the point at which both $\frac{dW}{dt} = 0$ and $\frac{dV}{dt} = 0$ and W and V are thus constant) away from the trajectory. This means the trajectory speeds up because the bottom of the trajectory it is not slowed as much by the equilibrium point, hence the increase in frequency. As shown by the voltage traces, the depolarizing currents only change the interburst duration (period of time between the driver potential bursts), which corresponds to the left hand region of the trajectory in the phase plane, where voltage is low. The actual burst duration, on the other hand, remains unchanged and even increases with $I_s = 100$nA. Correspondingly, in the phase planes, this is due to the equilibrium point rising towards the top right of the trajectory. The right hand end of the trajectory corresponds to a higher voltage. In the voltage trace, the bursts correspond to high voltages (above zero on the peak of the driver action potential). Thus, when the equilibrium in the phase plane moves toward the top right side of the trajectory, bursts will slow down and will spend more time at higher voltages at their peaks.

On the other hand, the hyperpolarizing current ($I_s < 0$nA) causes the red nullcline to lower and slightly flatten out, pulling the equilibrium point further toward the bottom left of the limit cycle. Therefore, the trajectory is are spending more time at lower voltages, hence the longer interburst durations in the voltage trace. Again, the burst durations remains unchanged because the top of the limit cylce is unchanged. When I_s becomes too negative (at $I_S = -35$nA), the equilibrium surpasses the limit cycle at $V = 0$mV and thus, the trajectory is unable to make a full cycle, hence the rhythmic firing disappears in the voltage trace.

Part 3. Modeling Mechanically-activated ion Channels

6. Introduction

As shown in Section 5, current injection in the single cell only reproduced **Component 2** of the stretch response, suggesting that the model needs refinement to capture stretch response **Components 1 and 3**. Therefore, we can introduce possible mechanosensitive channels into this model. As explained in Section 2.4, preliminary results have found mRNAs encoding several potential mechano-gated channels, specifically TREK-1 and Piezo-2 type channels in the CG system. Thus, in the next Sections, TREK-1 and Piezo-2 type channels are incorporated into the coupled and decoupled model systems to refine our model of the CG's stretch response. Since research in other organisms have found that TREK-1 and Piezo-2 behave differently from each other, we have created two independent current equations to model the currents of these channels. TREK-1 type channels will be included in the small cells in the coupled model system, while Piezo-2 type channels will be included in both the large and small cells.

7. TREK-1 Channel in Single Decoupled System

7.1. **Introduction.**

The TREK-1 type (TREK) channel is a potassium leak channel involved in mechanoelectrical feedback regulation. This channel behaves similarly to an outward leak channel with reversal potential of $-80mV$. For simplicity, this channel is modeled as an instantaneous ion leak channel, which opens upon stretch and is not time delayed. Therefore, it's conductance g_T is stretch sensitive.

However, as mentioned in Section 2.5, Honore (2006) found that this channels activation involves torque and shows pronounced desensitization after 100 ms. Thus, it is hypothesized that this channel is only active during the ramp phases of stretch (when torque is not equal to zero) [11]. The equation governing the dynamics of this channel is:

$$I_T = g_T(t)(V_A - V_T) \tag{5}$$

The function $g_T(t)$ is the conductance of the TREK channel, the variable V_A is the membrane potential of the large cells, and the variable V_T is the reversal potential of TREK channels.

There are two possible approaches this study focuses on in describing the mechanisms for the conductance of this channel:

Approach T1:
The conductance could be modeled as a simple step function, which biologically would suggest this channel simply opens whenever stretch torque is present. Mathematically, it can be thought of as having the stretch conductance proportional to the derivative of stretch. Thus, it is a step function proportional to the derivative of the slope of the stretch. It is a positive constant on ramp up, 0 during the hold, and a negative constant on the ramp down.

Approach T2:
Instead of an all or nothing effect, the channels could open as a function of the degree of applied stretch during the ramp, i.e., as more stretch is applied, more current would flow through the channel. Thus, the conductance function $g_T(t)$ can be modeled proportional to stretch torque and is positive and increasing on the ramp up, 0 during hold, and negative and increasing on the ramp down.

7.2. **Model Response to TREK Channel: Methods.**

To gain an understanding of how this channel behaves and modulates the output of the Morris-Lecar model system, we can incorporate it into the decoupled system, similarly to the way we incorporated a current to the system.

Example 2

Returning to the example used earlier, this table lists the parameters of the decoupled system with the TREK channel:

Single Decoupled System with I_T			
Parameter	Variable	Value Used	
Cell surface area, cm^2		0.001	
Total cell capacitance, nF	C	10	
Ca^{2+} reversal potential, mV	V_{Ca}	100	
K^+ reversal potential, mV	V_K	-80	
Leak reversal potential, mV	V_L	-10	
TREK reversal potential, mV	V_L	-80	
Ca^{2+} half activation slope, mV	V_1	0	
Ca^{2+} current activation slope, mV	V_2	15	
K^+ half activation slope, mV	V_3	0	
K^+ current activation slope, mV	V_4	15	
K^+ current minimum rate constant, ms	ϕ_W	0.002	
Ca^{2+} current maximal conductance, $\mu S/cm^2$	g_{Ca}	24	
K^+ current maximal conductance, $\mu S/cm^2$	g_K	64	
Ca^{2+} current maximal conductance, $\mu S/cm^2$	g_L	1	
Parameter	Variable	Min. Value Used	Max. Value Used
TREK channel maximal conductance, $\mu S/cm^2$	g_T	1	60

7.3. **Model Response to TREK Channel: Results.**

Figures 25-26 depict the voltage traces of the output from Example 2 affected by the TREK current I_T in approaches T1 and T2.

Example 2, modeling approach T1

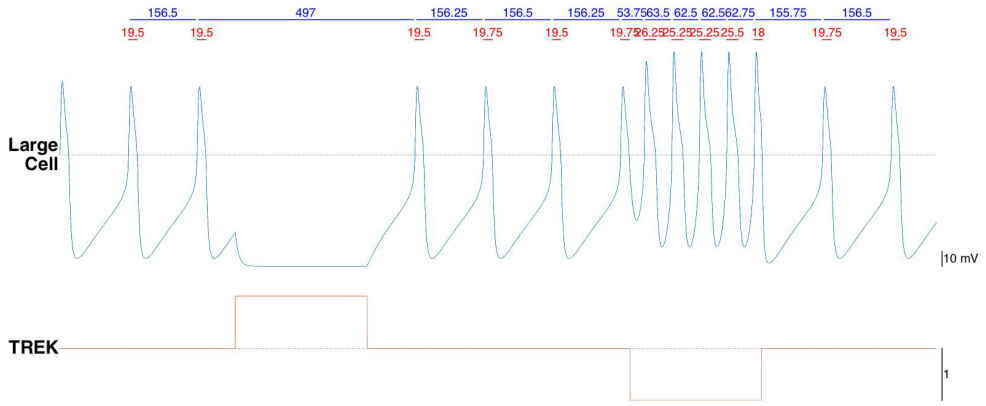

FIGURE 25. Voltage and conductance traces of Example 2, modeling approach T1 with $g_T = 12\mu S/cm^2$. The x-axis is a unitless time axis showing the same time scale in all figures. The blue numbers above the voltage trace correspond to the cycle period duration of each driver potential and the red numbers correspond to the burst durations.

Example 2, modeling approach T2

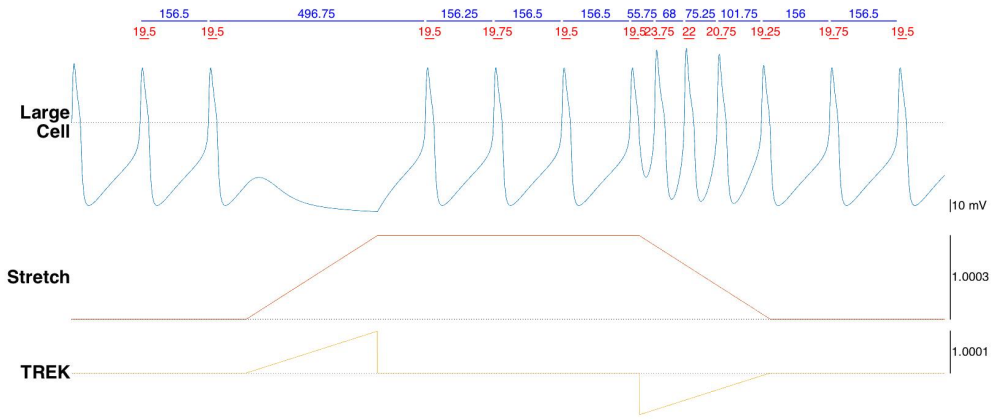

FIGURE 26. Voltage, stretch, and conductance traces of Example 2, modeling approach T2 with$g_T = 12\mu S/cm^2\mu$. The x-axis is a unitless time axis showing the same time scale in all figures. The blue numbers above the voltage trace correspond to the cycle period duration of each driver potential and the red numbers correspond to the burst durations.

7.4. **Model Response to TREK Channel: Conclusion.**

The mechanics of the TREK current, when introduced into the Morris Lecar Decoupled Model, produces **component 1** of the CG's stretch response (the phase delay).

Additionally, it is important to note that the two different ways stretch can be incorporated into the mechanics of the TREK channel lead to very similar responses in the output of the model (**Approaches T1 and T2**). Therefore, we will focus on the simpler approach and continue exploration with the conductance of the TREK channel modeled as a step function, proportional to the derivative of stretch.

Although **component 3** of the stretch response is experimentally less-well characterized than the other two components, it may be helpful to utilize this model to gain an understanding of the mechanism behind the phenomena. For example, allowing the TREK current to change sign may seem artificial, nevertheless, when we make g_T negative during release from stretch, the third component of the experimentally observed stretch response appears. This is depicted by the increase in the value that measures the burst durations upon the slope down from stretch, shown by the numbers in red font above voltage trace in figures 25 and 26. This might suggest that at rest, without stretch, some TREK channels are open as K^+ leak channels. Upon rising stretch, more TREK channels open because this channel is mechanosensitve, but these TREK channels desensitize upon the hold of stretch. During release from stretch, the TREK channels, that are normally open at baseline (without stretch) will temporarily close, hence the negation of this current during stretch release.

8. Piezo-2 Channel in Single Decoupled System

8.1. **Introduction.**

We have taken three different approaches, with varying levels of complexity, to model the Piezo-2 type channel (Piezo). **Approach P1** has sufficient complexity to capture the viscoelastic properties of the receptor muscle. This has the effect of smoothing the stretch function within the conductance. **Approaches P2 and P3** use simpler linear and step function approximations to the conductance.

Approach P1:

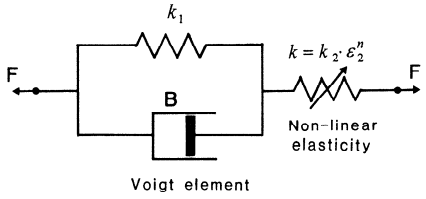

Figure 27. Diagram of the properties of the Piezo channel, Approach P1

We can model the Piezo channel according to a mathematical model of the crustacean stretch receptor neuron developed by Swerup and Rydqvist (1996). To mathematically describe the stretch receptor, the model was built off a model used to describe the viscoelastic properties of the receptor muscle and consists of a Voigt element (spring in parallel with the dashpot) in

series with a nonlinear spring, as shown in **Figure 27**. In this model system, due to the quick time scale, we assumed instantaneous adaptation to stretch [41].

The nonlinear differential equations governing the relations between tension and extension in the receptor muscles can be solved for a number of different simulations in the case of ramp-and-hold extension. The differential equations take the form:

During initial ramp phase $0 \leq t < t_1$:

$$\frac{d\epsilon_2}{dt} = \left([k_1(\alpha_P t) - k_1\epsilon_2 - k_2\epsilon_2^{n+1}]/B\right) + \alpha_P. \tag{6}$$

During the hold phase $t_1 \leq t < t_2$:

$$\frac{d\epsilon_2}{dt} = [k_1(\alpha_P t_1) - k_1\epsilon_2 - k_2\epsilon_2^{n+1}]/B. \tag{7}$$

During the end ramp $t_2 \leq t < t_3$:

$$\frac{d\epsilon_2}{dt} = \left([k_1\alpha_P(t_1 - t + t_2) - k_1\epsilon_2 - k_2\epsilon_2^{n+1}]/B\right) - \alpha_P. \tag{8}$$

Where the variable α_P is the rate of extension and fall, the variables t_1, t_2, and t_3 mark the end of the rising phase, beginning of the falling phase, and end of the falling phase, respectively, and the variable $\epsilon = \epsilon_1 + \epsilon_2$ is the total extension in the receptor.

For viscoelastic elements, the following parameters are constants: B is the viscous constant of the dashpot, k_1 and k_2 are the spring constants for linear and nonlinear springs, respectively, and n is the power constant for the nonlinear spring.

The extension ϵ_1 is used to define σ_m, the tension force divided by the cross-sectional area of the receptor muscle (m is the tension conversion). The following equation governs the relation between tension and extension in the receptor muscle:

$$\sigma_m = k_1 * \epsilon_1 + B * \frac{d\epsilon_1}{dt} \tag{9}$$

The open probability, P_o, for the mechanosensitive channel in the stretch receptor neuron depends on the tension σ_m and is governed by the following equation:

$$P_o = \left[1 + k_b * e^{[-s(\frac{\sigma_m}{m})^q]}\right]^{-1}. \tag{10}$$

For mechanosensitive channels, the following are constants: k_b is the Boltzmann constant, s is a sensitivity constant, q is the power constant, and is either set to 1 or 2. For simplicity, we assumed $q = 1$.

Therefore, the current due to Piezo:

$$I_P = P_o * g_P(V_A - V_P). \tag{11}$$

Where g_P is the total maximum stretch activated conductance. V_B and V_P are the reversal potential of the small cells and Piezo-2 Receptor, respectively.

Approaches P2 and P3:

To explore simpler alternatives, we can also model Piezo as a mechanosensitive non-specific cation channel that opens as a function proportional to stretch (**approach P2**) or opens as a step function (**approach P3**). In both cases, the equation governing the current through the

Piezo channel takes the following form:

$$I_P = g_P(t)(V_A - V_P) \tag{12}$$

Where the function $g_P(t)$ is the conductance of the Piezo channel, the variable V_A is the membrane potential of the large cells, and the variable V_P is the reversal potential of Piezo channels.

8.2. **Model Response to Piezo Channel: Methods.**

To gain an understanding of how this channel behaves and modulates the output of the Morris-Lecar model system, we can incorporate it into the decoupled system, similarly to the way we incorporated a current to the system.

Example 3

Returning to Example 1, used earlier, this table lists the parameters of the decoupled system with the Piezo channel:

Coupled Motor Pattern with I_T			
Parameter	Variable	Value Used	
Cell surface area, cm^2		0.001	
Total cell capacitance, nF	C	10	
Ca^{2+} reversal potential, mV	V_{Ca}	100	
K^+ reversal potential, mV	V_K	-80	
Leak reversal potential, mV	V_L	-10	
TREK reversal potential, mV	V_L	-80	
Ca^{2+} half activation slope, mV	V_1	0	
Ca^{2+} current activation slope, mV	V_2	15	
K^+ half activation slope, mV	V_3	0	
K^+ current activation slope, mV	V_4	15	
K^+ current minimum rate constant, ms	ϕ_W	0.002	
Ca^{2+} current maximal conductance, $\mu S/cm^2$	g_{Ca}	24	
K^+ current maximal conductance, $\mu S/cm^2$	g_K	64	
Ca^{2+} current maximal conductance, $\mu S/cm^2$	g_L	1	
Spring constant for linear spring, kPa	k_1	400	
Spring constant for nonlinear spring	k_2	2,200	
Power constant nonlinear spring	n	2	
Dashpot constant,kPa-ms	B	12,000	
Boltzmann constant (linear)	k_b	106	
Sensitivity constant (linear), kPa^{-1}	s	2.77	
Power constant (linear)	q	1	
Tension conversion factor	m	61.6	
Parameter	Variable	Min. Value Used	Max. Value Used
Piezo channel maximal conductance, $\mu S/cm^2$	g_P	1	30

8.3. **Model Response to Piezo Channel in the voltage trace: Results.**

Figures 28-30 depict the voltage traces of the output from Example 3 affected by the Piezo current I_P in approaches P1, P2, and P3.

Example 3, modeling approach P1

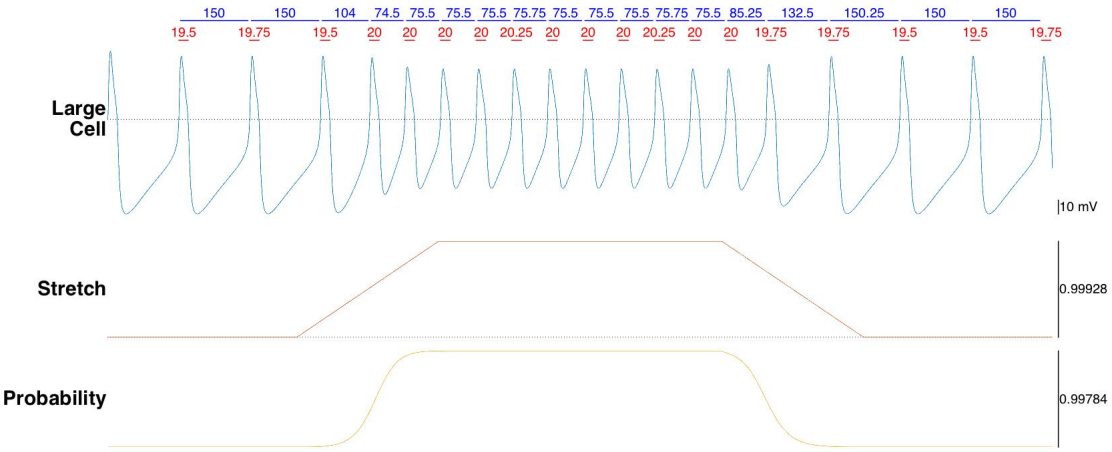

FIGURE 28. Voltage, stretch, and conductance traces of Example 3, modeling approach P1 with $g_P = 3\mu S/cm^2$. The x-axis is a unitless time axis showing the same time scale in all figures. The blue numbers above the voltage trace correspond to the cycle period duration of each driver potential and the red numbers correspond to the burst durations.

Example 3, modeling approach P2

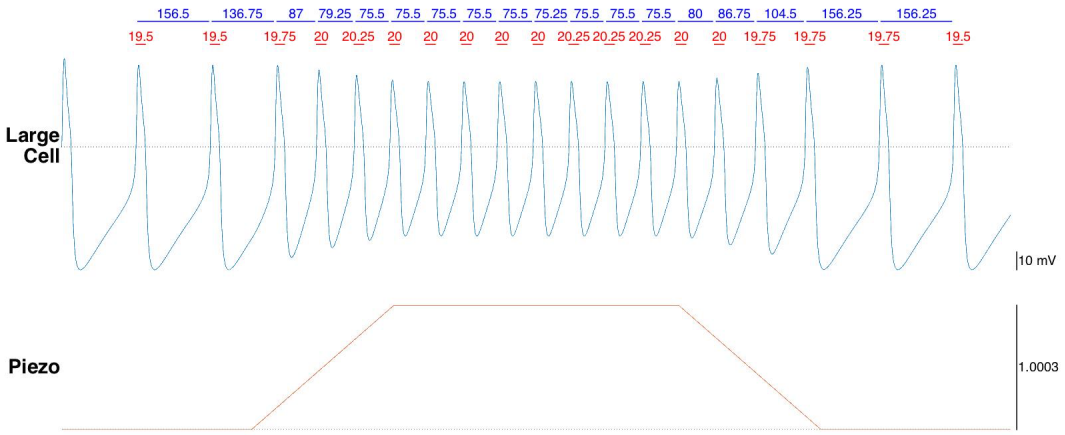

FIGURE 29. Voltage and conductance traces of Example 3, modeling approach P2 with $g_P = 3\mu S/cm^2$. The x-axis is a unitless time axis showing the same time scale in all figures. The blue numbers above the voltage trace correspond to the cycle period duration of each driver potential and the red numbers correspond to the burst durations.

Example 3, modeling approach P3

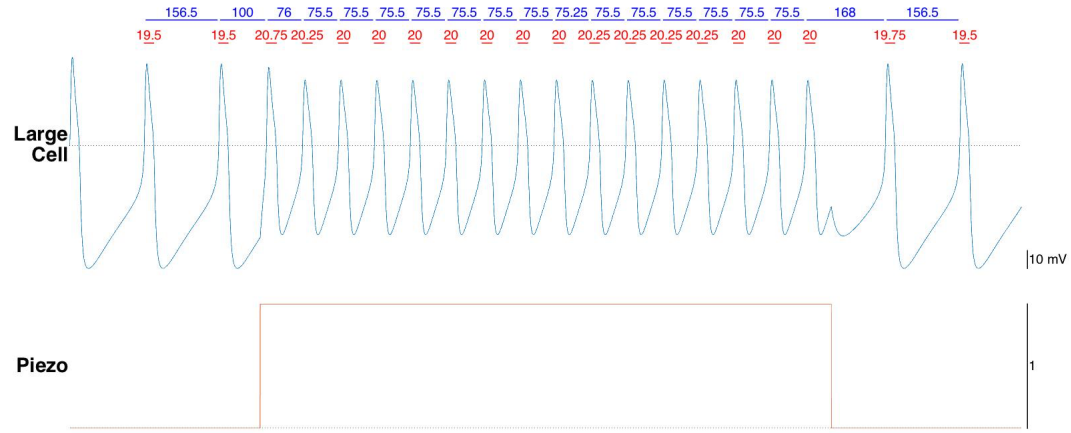

FIGURE 30. Voltage and conductance traces of Example 3, modeling approach P3 with $g_P = 3\mu S/cm^2$. The x-axis is a unitless time axis showing the same time scale in all figures. The blue numbers above the voltage trace correspond to the cycle period duration of each driver potential and the red numbers correspond to the burst durations.

8.4. **Model Response to Piezo Channel in the voltage trace: Conclusion.**

The mechanics of the Piezo current, when introduced into the Morris Lecar Decoupled Model, produces **component 2** of the CG's stretch response (increase in frequency). This response is very similar to the effects depolarizing current has on the system, shown in Section 2.

Additionally, it is important to note that the three approaches to incorporating stretch into the mechanics of the Piezo channel lead to very similar responses in the output of the model. However, the change in frequency is almost instantaneous in **approach P3** and more gradual in **approaches P1 and P2**.

9. TREK and Piezo in Single Decoupled System

9.1. **Introduction and Methods.**

As explained in Section 6, it is hypothesized that in order to produce all three stretch response components, more than one mechanosensitive channel must be present, two of which may be Piezo and TREK channels. To gain an understanding of how these channel interact to modulate the output of the Morris-Lecar model system, we can combine the approaches and parameter set of Sections 7 and 8 to incorporate the two channel types into the decoupled system together.

Example 4

Returning to Examples 2 and 3, the tables in Sections 7 and 8 list the parameters of the decoupled system with the TREK and Piezo channels.

9.2. **Model Response to TREK and Piezo Channels in the voltage trace: Results.**

Figures 31-33 depict the voltage traces of the output from the example decoupled model network affected by both TREK and Piezo channels. Each figure has the same TREK channel, but different approaches to modeling the Piezo channel are used, labeled accordingly.

Example 4, modeling approach P1

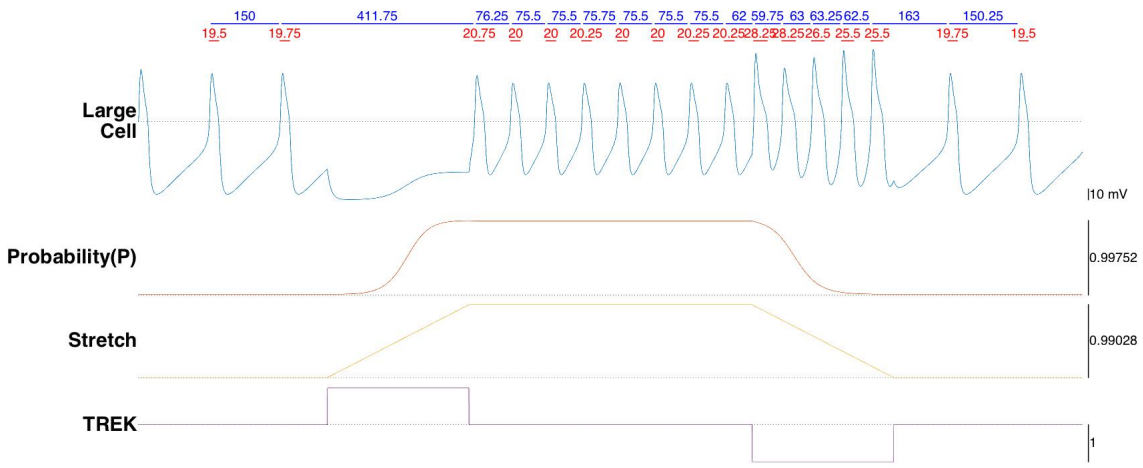

FIGURE 31. Voltage, Piezo conductance, stretch, and TREK conductance traces of Example 4, modeling approach P1 with $g_P = 3\mu S/cm^2$ and $g_T = 12\mu S/cm^2$. The x-axis is a unitless time axis showing the same time scale in all figures. The blue numbers above the voltage trace correspond to the cycle period duration of each driver potential and the red numbers correspond to the burst durations.

Example 4, modeling approach P2

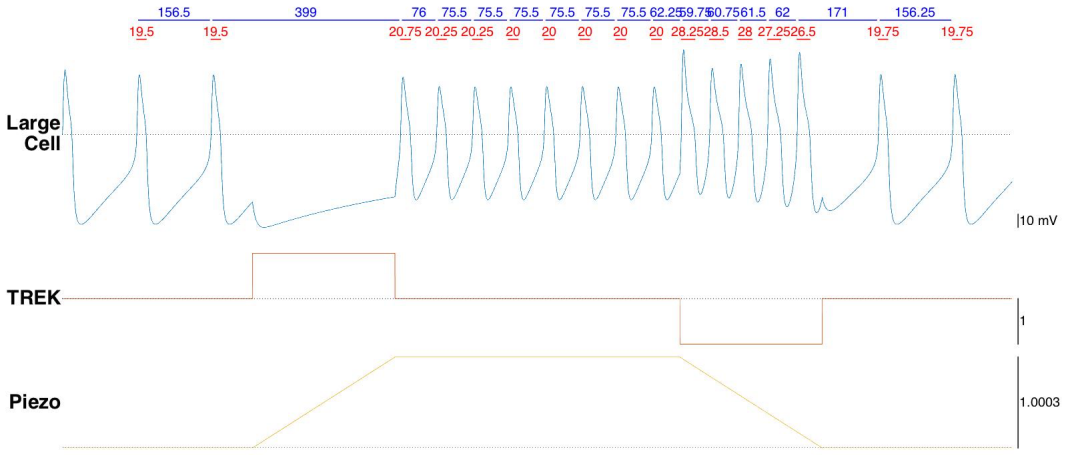

FIGURE 32. Voltage and conductance traces of Example 4, modeling approach P2 with $g_P = 3\mu S/cm^2$ and $g_T = 12\mu S/cm^2$. The x-axis is a unitless time axis showing the same time scale in all figures. The blue numbers above the voltage trace correspond to the cycle period duration of each driver potential and the red numbers correspond to the burst durations.

Example 4, modeling approach P3

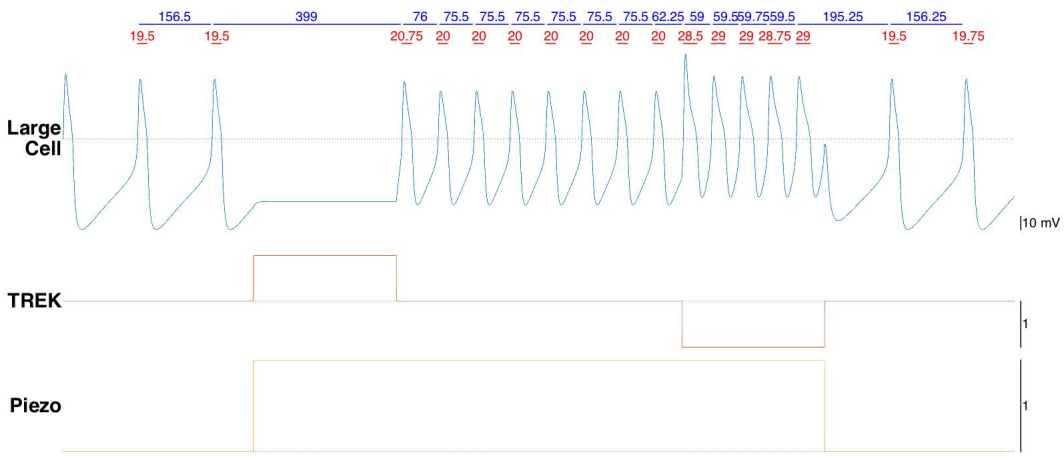

FIGURE 33. Voltage and conductance traces of Example 4, modeling approach P3 with $g_P = 3\mu S/cm^2$ and $g_T = 12\mu S/cm^2$. The x-axis is a unitless time axis showing the same time scale in all figures. The blue numbers above the voltage trace correspond to the cycle period duration of each driver potential and the red numbers correspond to the burst durations.

9.3. **Model Response to TREK and Piezo Channels in the phase portrait: Results.**

To gain an understanding of how single cell behavior changes via the opening and closing of the TREK and Piezo channels when the CG is stretched, we can analyze the phase planes, indicating changes to patterns in the CG's organized output.

Figures 34-47 depict the phase planes of the same example parameter set with no channels, TREK channel, Piezo channels, and combinations of the two channels opened with constant conductance. Through exploring the nullclines configuration for each combination of open channels, we can gain a better understanding of the modulation by the channel on the CG's output. Figures 34-47 are organized to show the competing impact of open TREK and Piezo channels during the ramp up and down phases of stretch.

Phase portrait without stretch

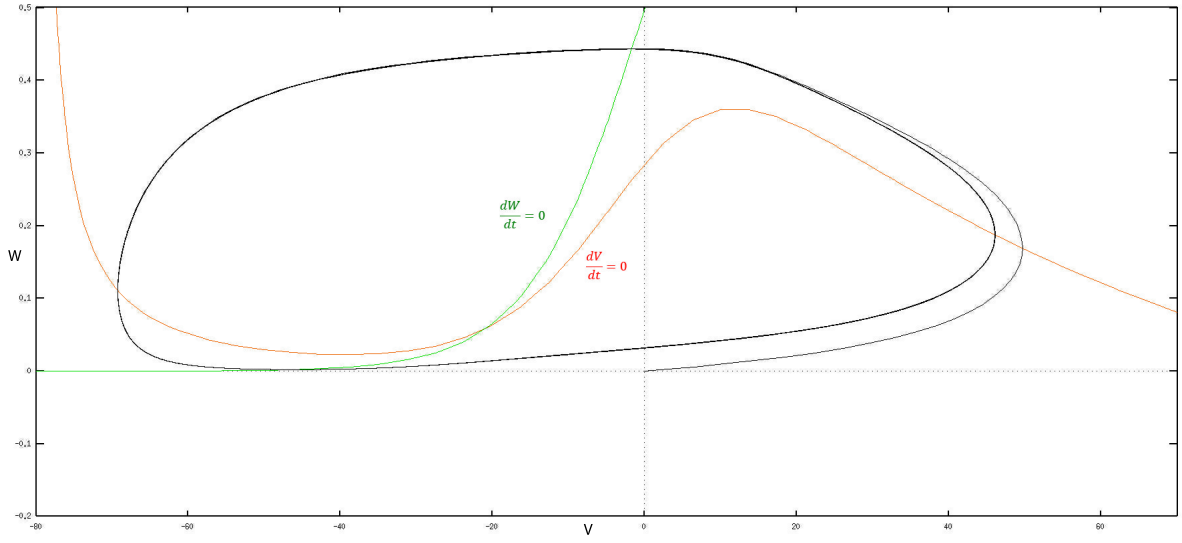

FIGURE 34. Phase portrait of Example 4 with g_T and $g_P = 0\ \mu S/cm^2$.

Phase portraits during ramp up and ramp down of stretch: Piezo only

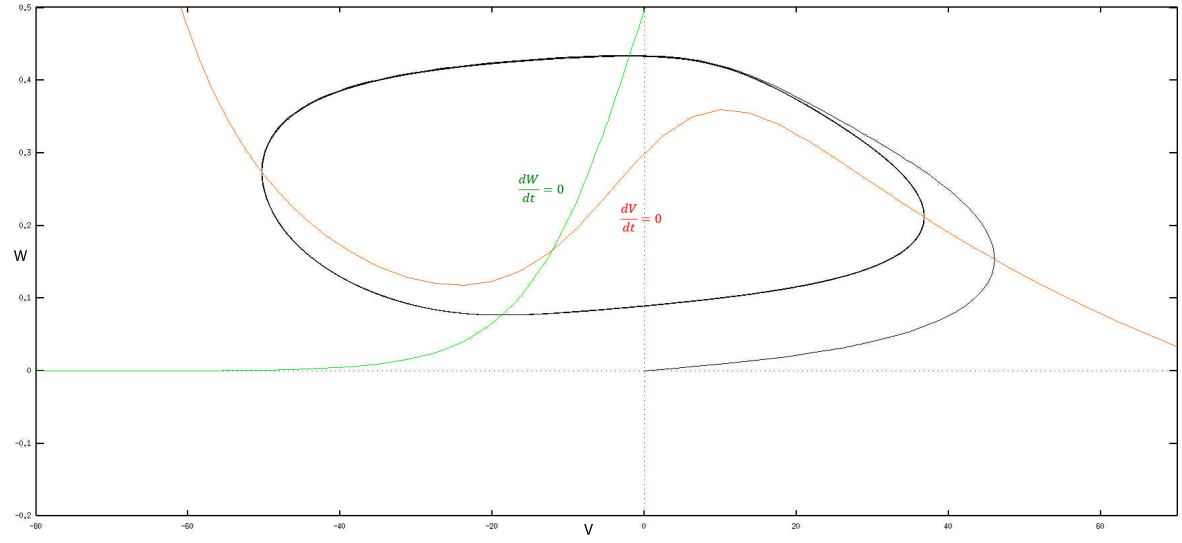

FIGURE 35. Phase portrait of Example 4 with $g_T = 0\ \mu S/cm^2$ and $g_P = 3\ \mu S/cm^2$.

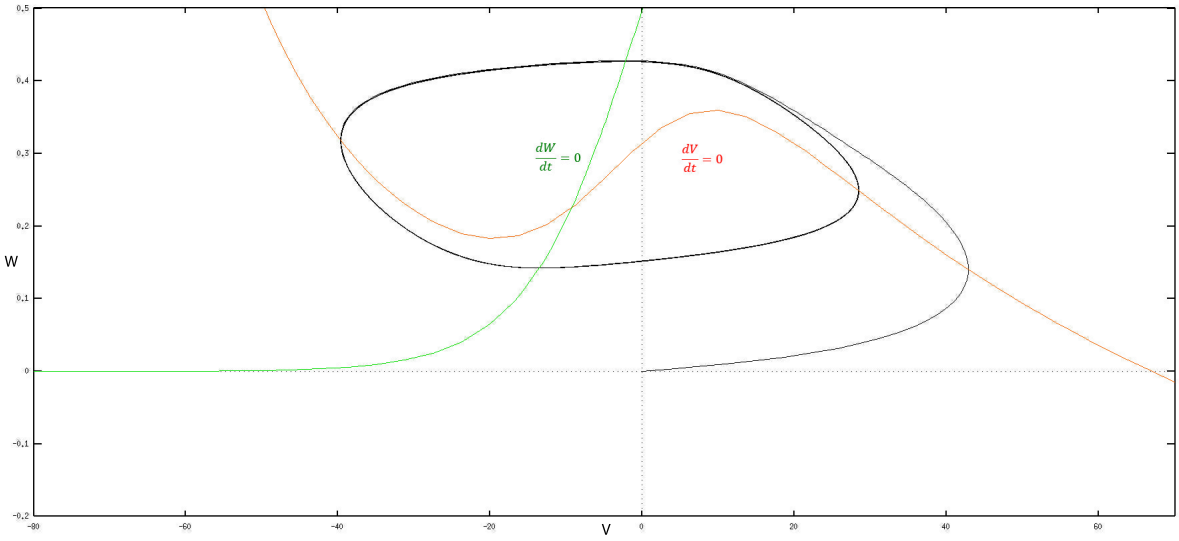

FIGURE 36. Phase portrait of Example 4 with $g_T = 0\ \mu S/cm^2$ and $g_P = 6\ \mu S/cm^2$.

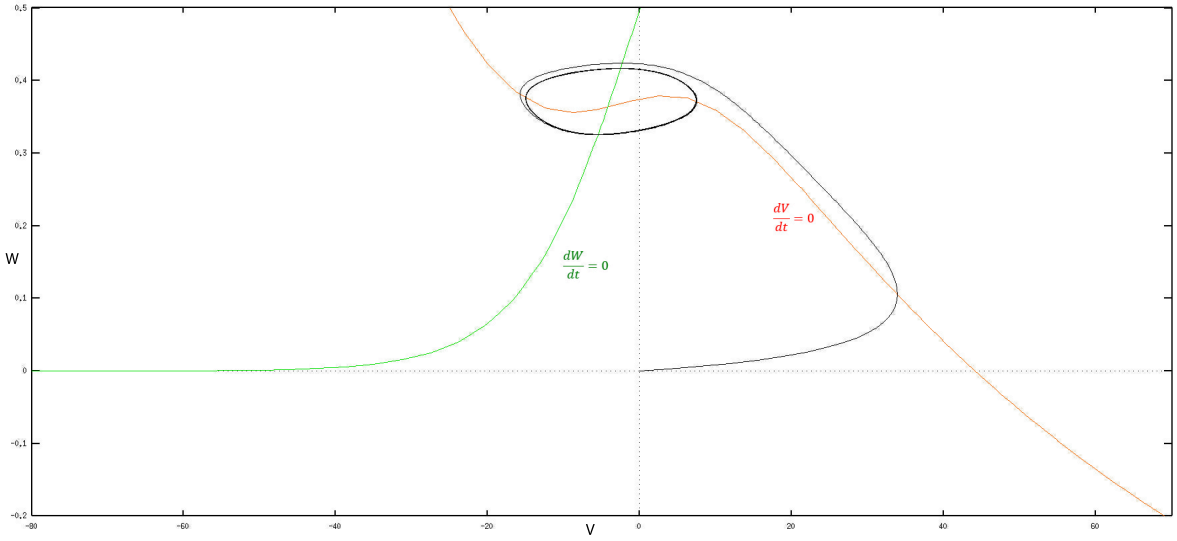

FIGURE 37. Phase portrait of Example 4 with $g_T = 0\ \mu S/cm^2$ and $g_P = 18\ \mu S/cm^2$.

Phase portraits during ramp up of stretch: TREK only

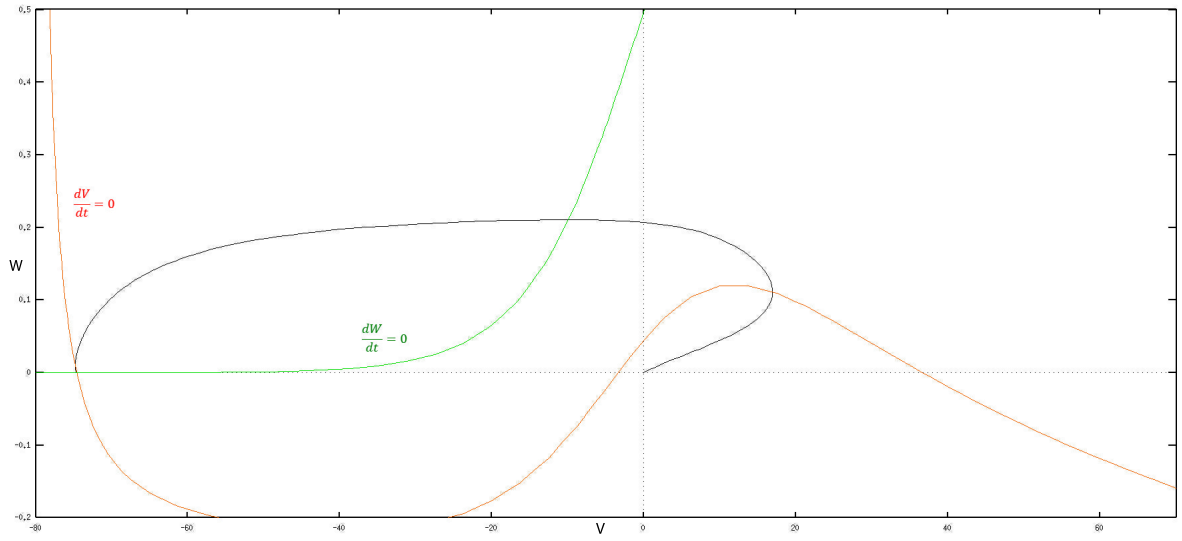

FIGURE 38. Phase portrait of Example 4 with $g_T = 12\ \mu S/cm^2$ and $g_P = 0\ \mu S/cm^2$.

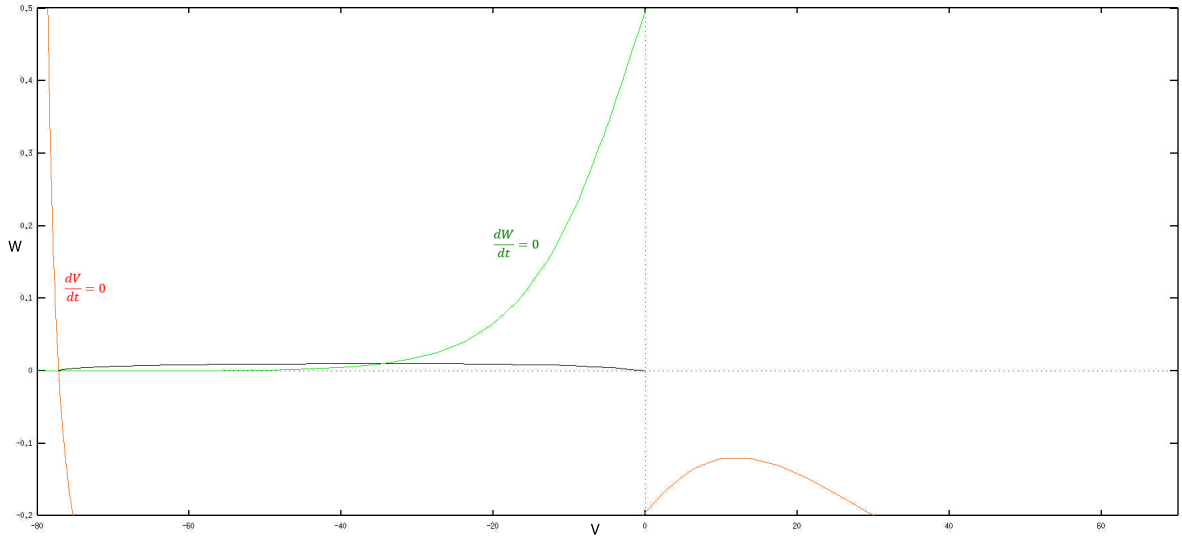

FIGURE 39. Phase portrait of Example 4 with $g_T = 24\ \mu S/cm^2$ and $g_P = 0\ \mu S/cm^2$.

Phase portraits during ramp up of stretch: TREK and Piezo together

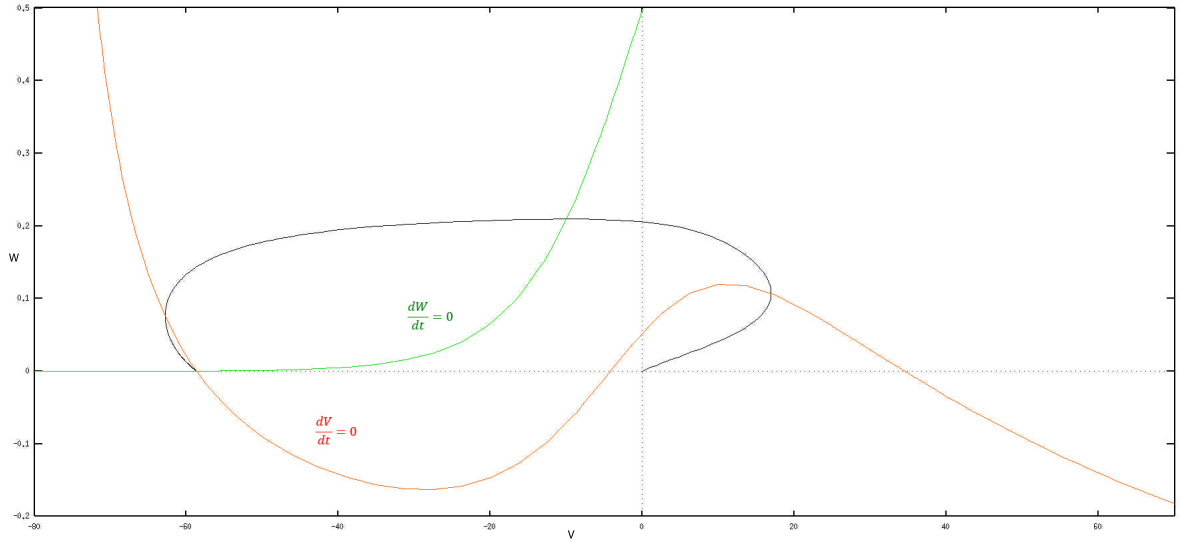

FIGURE 40. Phase portrait of Example 4 with $g_T = 12\ \mu S/cm^2$ and $g_P = 1.5\ \mu S/cm^2$.

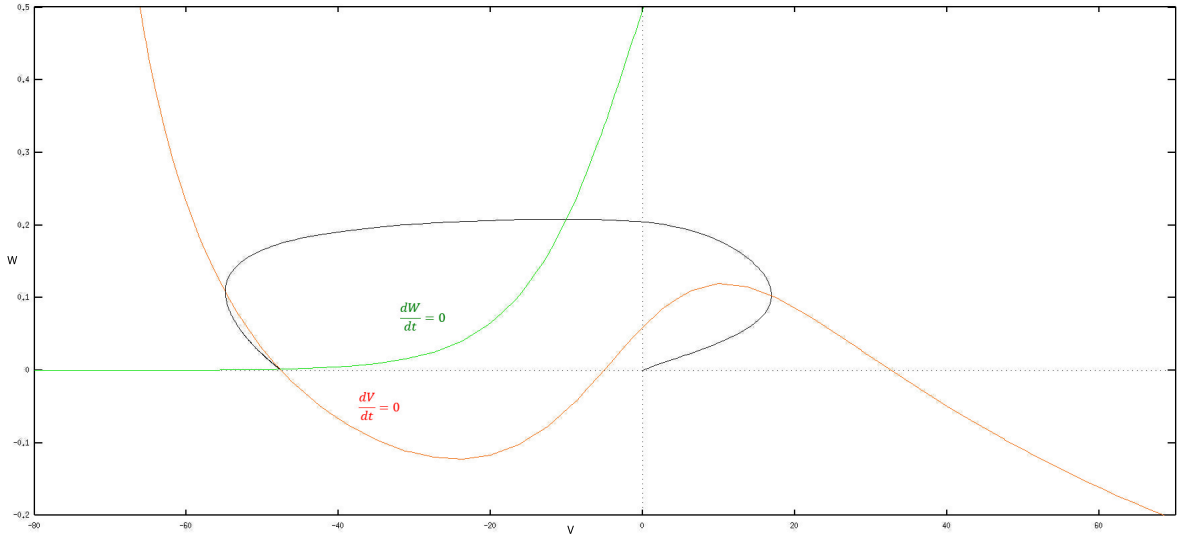

FIGURE 41. Phase portrait of Example 4 with $g_T = 12\ \mu S/cm^2$ and $g_P = 3\ \mu S/cm^2$.

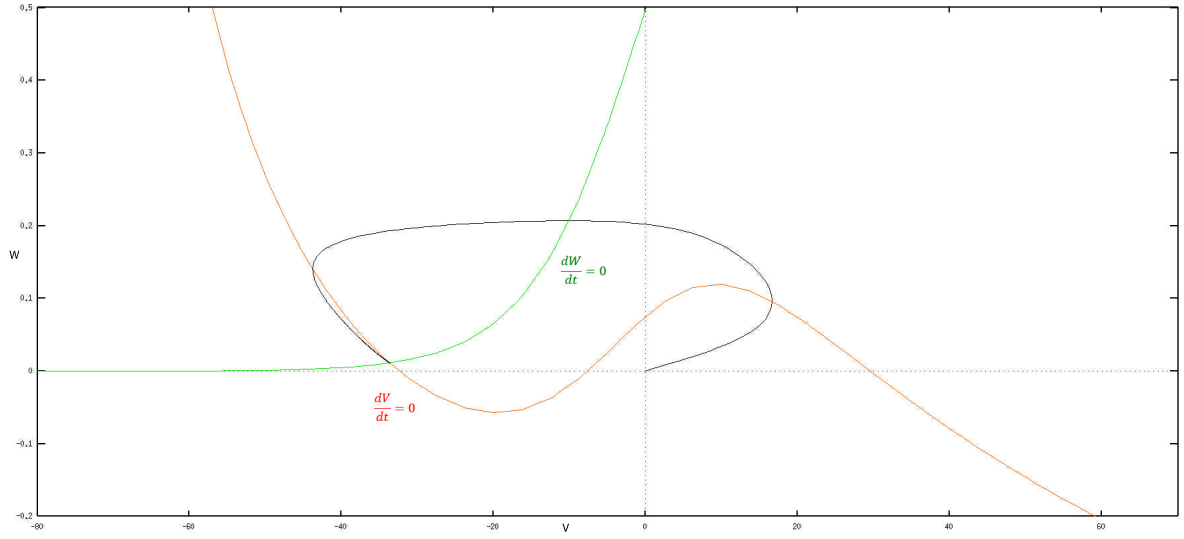

FIGURE 42. Phase portrait of Example 4 with $g_T = 12\ \mu S/cm^2$ and $g_P = 6\ \mu S/cm^2$.

Phase portraits during ramp down from stretch: TREK only

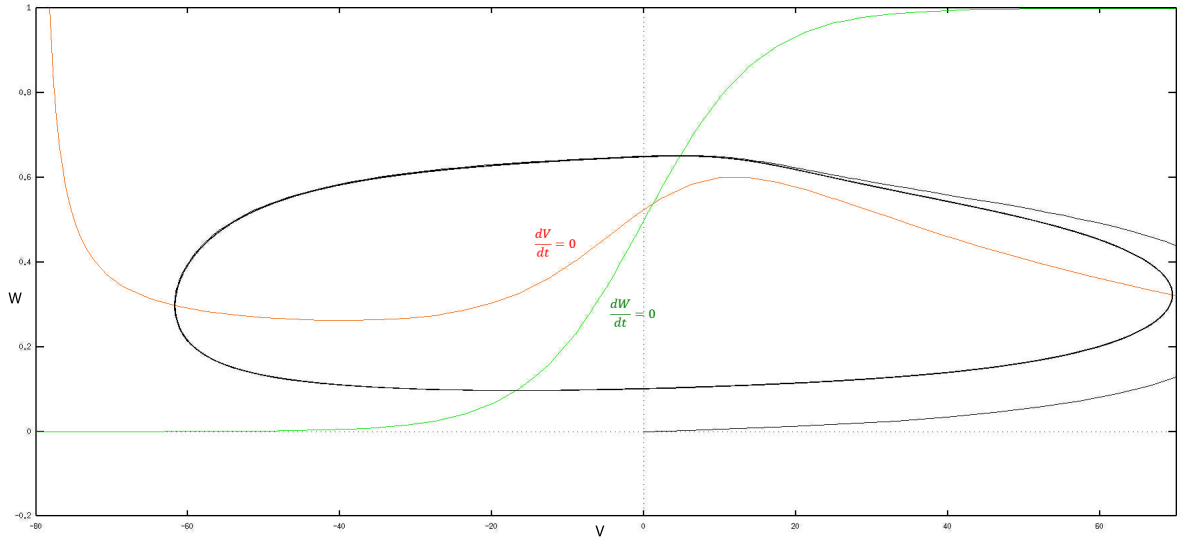

FIGURE 43. Phase portrait of Example 4 with $g_T = -12\ \mu S/cm^2$ and $g_P = 0\ \mu S/cm^2$.

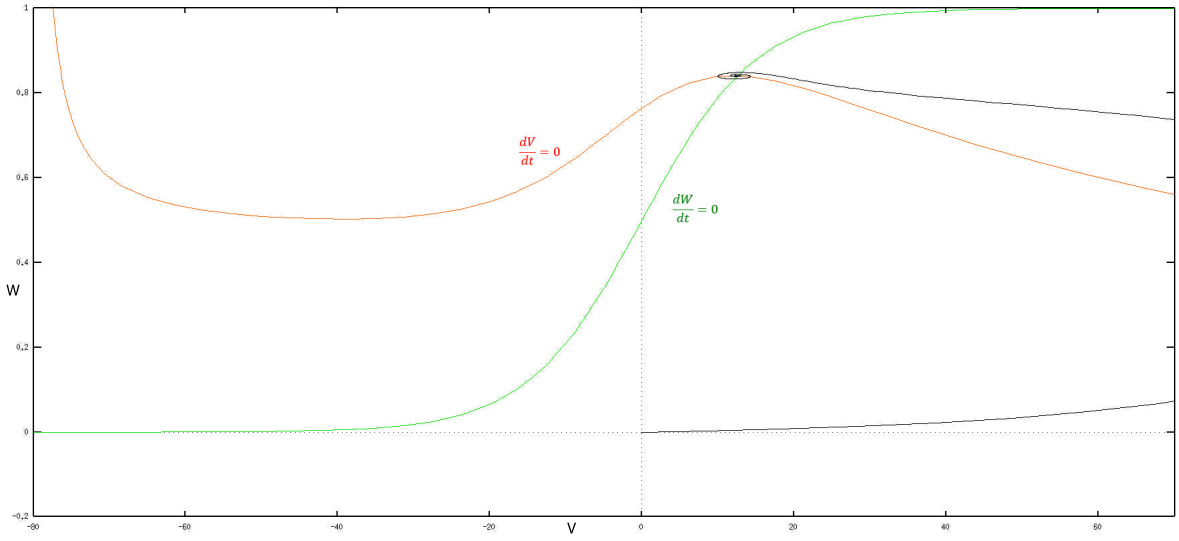

FIGURE 44. Phase portrait of Example 4 with $g_T = -24\ \mu S/cm^2$ and $g_P = 0\ \mu S/cm^2$.

Phase portraits during ramp down from stretch: TREK and Piezo together

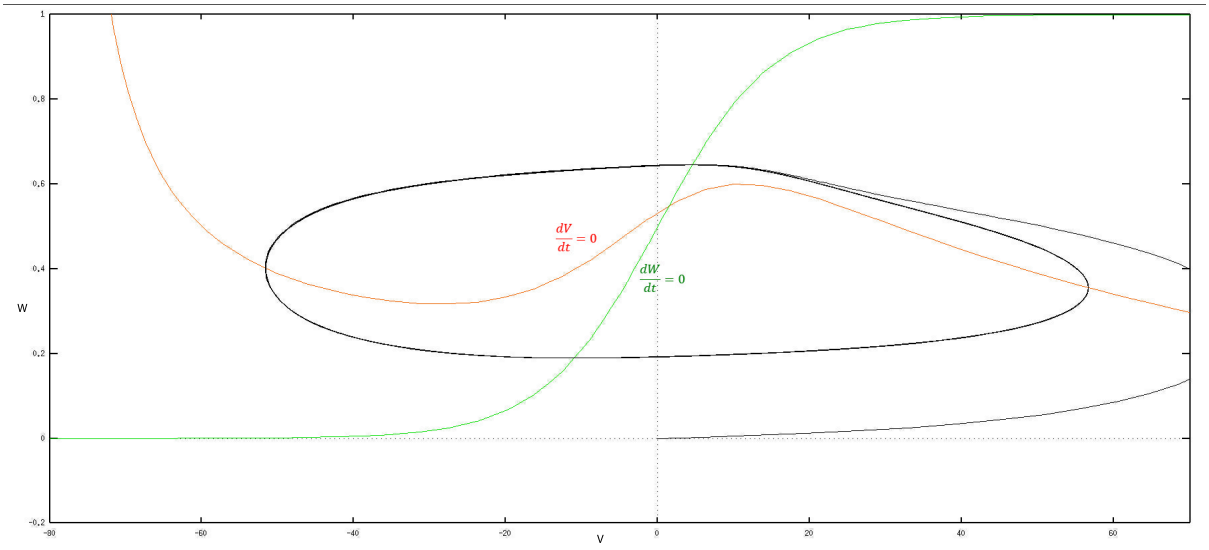

FIGURE 45. Phase portrait of Example 4 with $g_T = -12\ \mu S/cm^2$ and $g_P = 1.5\ \mu S/cm^2$.

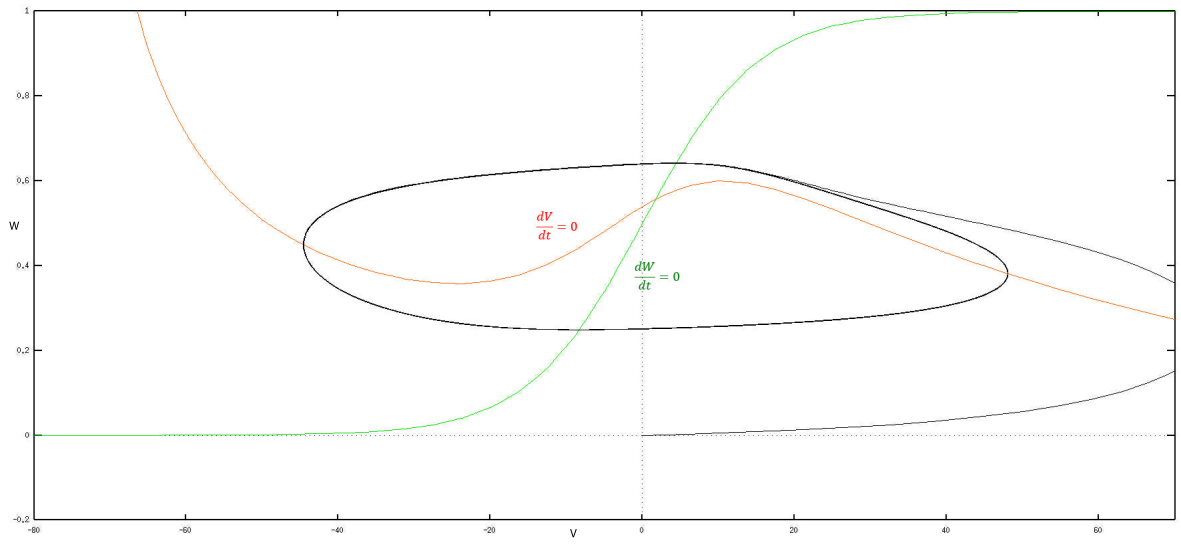

FIGURE 46. Phase portrait of Example 4 with $g_T = -12\ \mu S/cm^2$ and $g_P = 3\ \mu S/cm^2$.

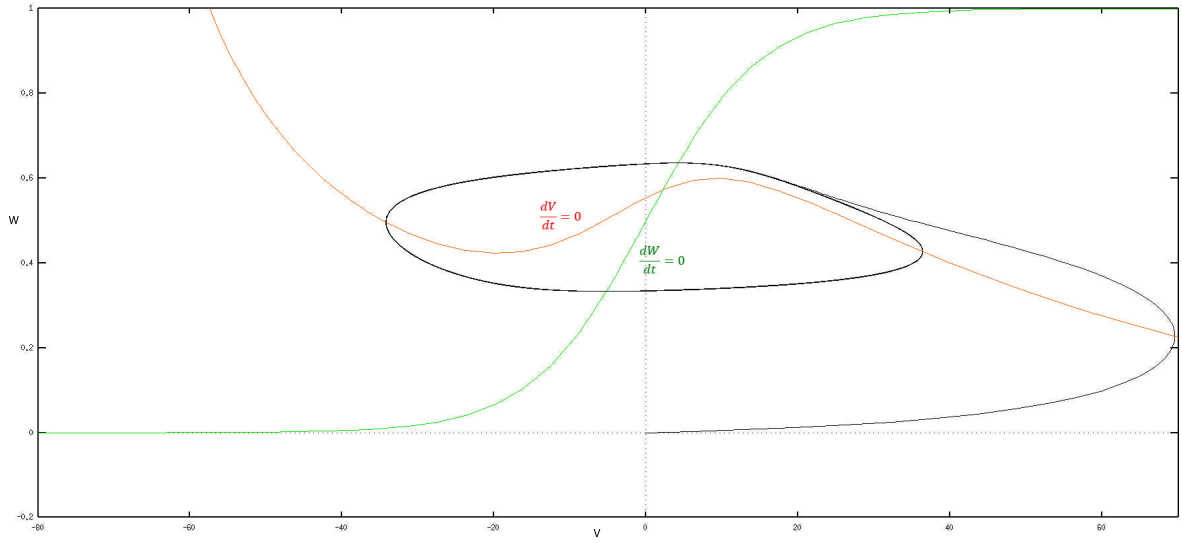

FIGURE 47. Phase portrait of Example 4 with $g_T = -12\ \mu S/cm^2$ and $g_P = 6\ \mu S/cm^2$.

9.4. **Model Response to TREK and Piezo Channels: Conclusion.**

Ramp up of stretch

During the ramp up of the stretch, we hypothesized that the Piezo channel could open as a step function, a function proportional to stretch, or through a complex mechanism modeling the probability of channel opening. Similarly to the effect of the depolarizing current injection on both the voltage traces and the nullclines of the single cell model system, in all three approaches to modeling the Piezo channel, the Piezo current causes the equilibrium to shift away from the limit cycle trajectory. This explains the increase in frequency: the limit cycle speeds up because the equilibrium lies farther away from it. However, unlike the depolarizing current injections, the limit cycle shrinks as the conductance g_P increases, which corresponds to the smaller amplitude of the driver potential bursts, as shown in the voltage trace. Since everything shrinks together, the frequency of the bursts increases drastically.

Additionally, during the ramp up of the stretch, we hypothesized that TREK channels open as a step function proportional to the derivative of the stretch or as a function of proportional to stretch torque. Similar to the effect of the hyperpolarizing current injection on both the voltage trace and the nullcline of the single cell model system, the current due to TREK with the conductance $g_T > 0\ \mu S/cm^2$ has a huge effect on moving the equilibrium toward the bottom left of the limit cycle trajectory, an area of low voltage and the voltage near the interburst periods. Therefore, since the system is spending more time at low voltages, the interburst interval is increases, as shown by the voltage traces. When g_T becomes very large, the equilibrium surpasses the bottom of the nullcline, similarly to when the hyperpolarizing current becomes very negative. Thus, the trajectory is unable to complete the cycle, the system is prevented from bursting, and equilibrates at a low voltage. Hence, in the voltage trace, the network stops bursting.

Since we suspect that both these channels are opening on the ramp up of stretch, we can look at the nullclines with both channels open. During the ramp up, Piezo pulls the equilibrium away from the bottom of the limit cycle, while TREK pulls the equilibrium towards and beyond the limit cycle trajectory. Thus, as shown by these nullclines, TREK seems to be outcompeting Piezo. Hence, we see the phase delay or temporary loss of bursting, a phenomenon due to the TREK, as explained above.

Ramp down of stretch

As g_P decreases during ramp down, the Piezo channels gradually close and the equilibrium that starts out far away from the limit cycle trajectory gradually comes down to return closer to the left bottom of the limit cycle.

Modeling TREK during ramp down as a step function with negative g_T causes the nullcline to behave similarly in the depolarizing current example. There is an increase in frequency, shown by the voltage trace. Additionally, since the TREK channel has such a powerful influence on changing the equilibrium, the equilibrium is pulled all the way towards the top right of the limit cycle, to an area of higher voltage. Thus, the limit cycle spends more time at the higher voltage, which corresponds to the peaks of the bursting spikes. Therefore, as shown in the voltage trace, the bursts will spend more time at the higher voltage peaks, corresponding to the increase in burst duration. When g_T becomes very negative, the limit cycle disappears in a bifurcation, and the system equilibrates at a high voltage equilibrium. This would correspond to a plateau in the voltage trace, which has not been observed experimentally.

Since we suspect that both these channels are open on the ramp down, we can look at the nullclines with both channels present. During the ramp down, Piezo is closing and thus pulls the equilibrium from the middle of the limit cycle back to baseline and the trajectory becomes larger. This phenomenon competes with the powerful TREK, which pulls the equilibrium even closer towards the top right of the limit. Since the nullclines of the system with both trajectories show the equilibrium being pulled toward the higher voltage at the top of the limit cycle, TREK seems to be outcompeting Piezo, but the moderating effect of Piezo is sufficient to prevent the loss of the limit cycle, and the associated voltage plateau, that occurs with TREK only. Longer time spent at high voltage corresponds to more time spent at the peaks of the bursts, hence we see the increase in burst period in the voltage-trace.

Part 4. Two Coupled Morris-Lecar Model

10. Current Injection

10.1. Model Response to Current: Methods.

Now we reintroduce the large cells with electrical and chemical coupling. As a single cell model, to explore the possible effects of stretch through stretch sensitive ion channels in the coupled system, we start by simulating a current injection experiment. In Section 11, we move on to incorporating stretch sensitive channels into the two-cell model. The equations governing Morris-Lecar dynamics of a two-cell-type system with current injection (I_s) are as given in Section 4.1, except equation 2 is changed to equation 13 below with all other equations are unchanged:

$$C\frac{dV^A}{dt} = -g_L^A(V^A - V_L) - g_{Ca}^A M_\infty(V^A - V_{Ca}) - g_K^A W(V^A - V_K) - g_{Syn}^A S_\infty(V^B)(V^A - V_{Syn}) - g_{gap}(V^A - V^B) + I_s. \tag{13}$$

Current is applied to the large cells only, since in the current injection experiments, only the large cells are injected with current. By varying this additional current, this model will show the possible effects of hyperpolarizing and depolarizing current on the coupled Morris-Lecar Model. As the number of variables increases, the geometry becomes harder to visualize, so we do not plot the (4 dimensional) phase portraits. Ongoing work in the lab is aimed at alternative ways to visualize the geometric interaction between the nullclines of the two cells.

Example 5

Let's take the same parameter set used in Example 2 for the decoupled model, but now reintroduce the coupled small cells, with chemical and electrical coupling, and apply current I_s to the large cells:

Coupled Motor Pattern with I_s			
Parameter	Variable	Value Used	
Cell surface area, cm^2		0.001	
Total cell capacitance, nF	C	10	
Ca^{2+} reversal potential, mV	V_{Ca}	100	
K^+ reversal potential, mV	V_K	-80	
Leak reversal potential, mV	V_L	-10	
Synaptic reversal potential, mV	V_{syn}	-15	
Ca^{2+} half activation slope, mV	V_1	0	
Ca^{2+} current activation slope, mV	V_2	15	
K^+ half activation slope, mV	V_3	0	
K^+ current activation slope, mV	V_4	15	
Synaptic half activation slope, mV	V_5	0	
Synaptic current activation slope, mV	V_6	5	
K^+ current minimum rate constant, ms	ϕ_W	0.002	
Ca^{2+} current maximal conductance, $\mu S/cm^2$	g^A_{Ca}	24	
K^+ current maximal conductance, $\mu S/cm^2$	g^A_K	64	
Ca^{2+} current maximal conductance, $\mu S/cm^2$	g^A_L	1	
Chemical synaptic strength, $\mu S/cm^2$	g^A_{syn}	18	
Ca^{2+} current maximal conductance, $\mu S/cm^2$	g^B_{Ca}	49	
K^+ current maximal conductance, $\mu S/cm^2$	g^B_K	60	
Ca^{2+} current maximal conductance, $\mu S/cm^2$	g^B_L	6	
Chemical synaptic strength, $\mu S/cm^2$	g^B_{syn}	35	
Electrical coupling strength, $\mu S/cm^2$	g_{gap}	28	
Parameter	Variable	Min. Value Used	Max. Value Used
Stretch Current,nA	I_s	-175	500

10.2. **Model Response to Current: Results.**

Figures 48-53 depict the large and small cell voltage traces from Example 5 affected by the current I_s.

Depolarizing Current ($I_s > 0$nA)

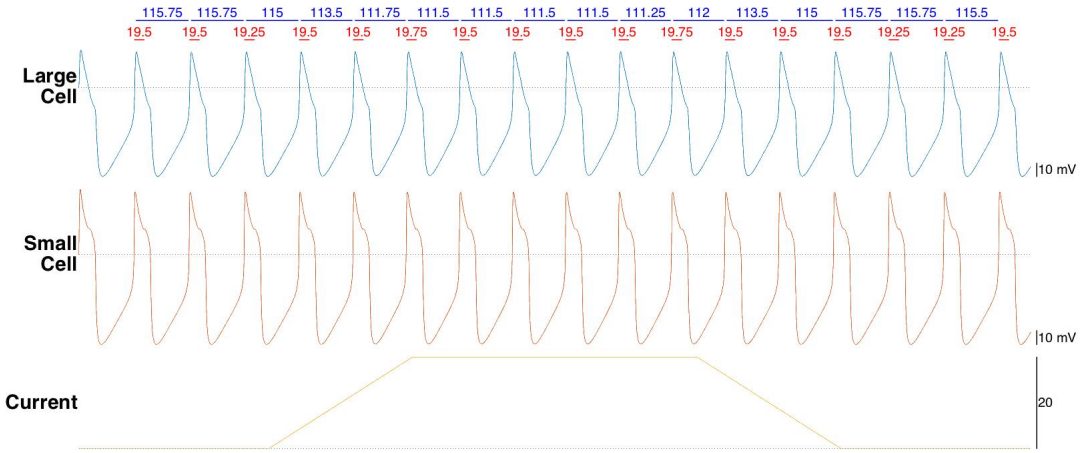

FIGURE 48. Voltage and current traces of Example 5 with $I_s = 20$nA. The x-axis is a unitless time axis showing the same time scale in all figures. The blue numbers above the voltage trace correspond to the cycle period duration of each large cell driver potential and the red numbers correspond to the burst durations.

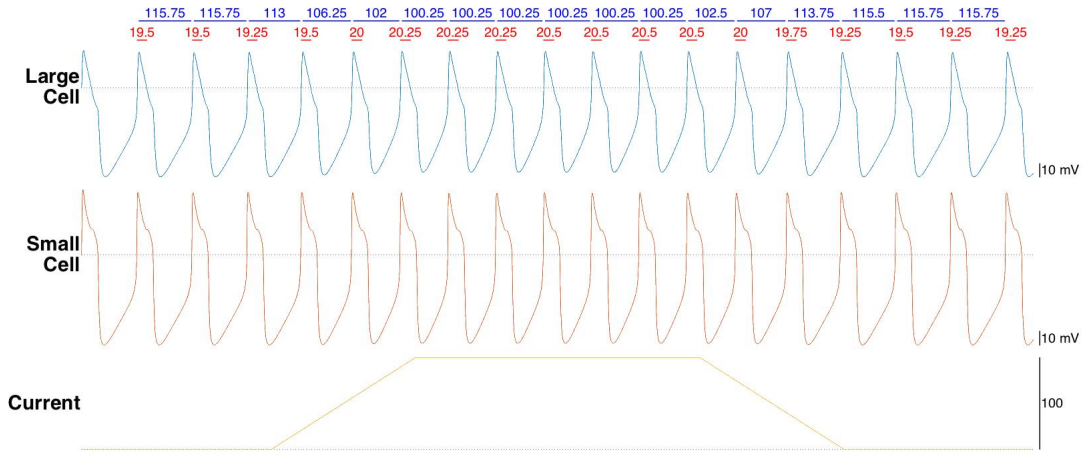

FIGURE 49. Voltage and current traces of Example 5 with $I_s = 100$nA. The x-axis is a unitless time axis showing the same time scale in all figures. The blue numbers above the voltage trace correspond to the cycle period duration of each large cell driver potential and the red numbers correspond to the burst durations.

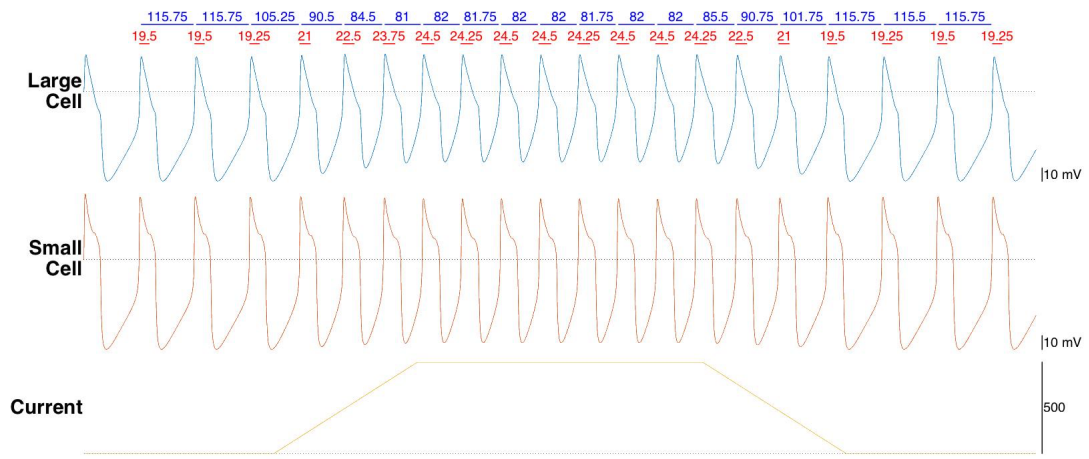

FIGURE 50. Voltage and current traces of Example 5 with $I_s = 500$nA. The x-axis is a unitless time axis showing the same time scale in all figures. The blue numbers above the voltage trace correspond to the cycle period duration of each large cell driver potential and the red numbers correspond to the burst durations.

Hyperpolarizing Current ($I_s < 0$nA)

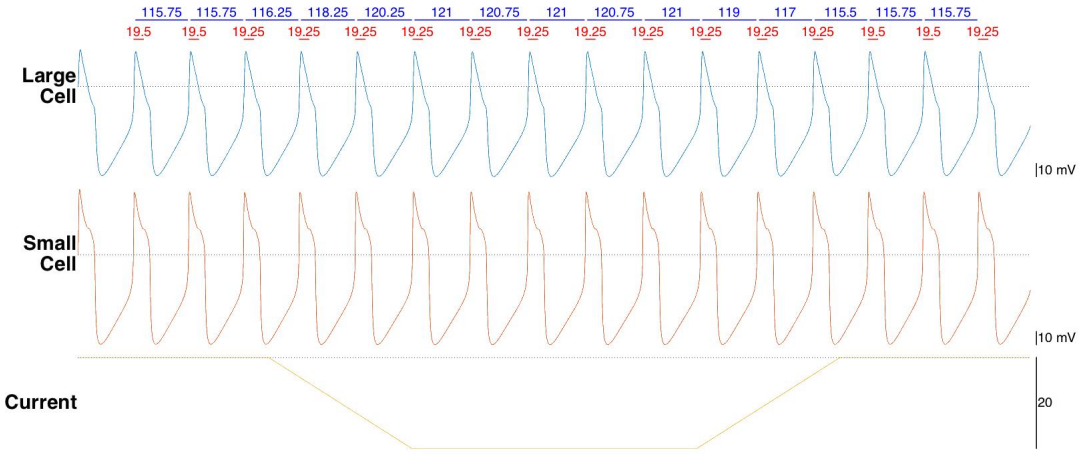

FIGURE 51. Voltage and current traces of Example 5 with $I_s = -20$nA. The x-axis is a unitless time axis showing the same time scale in all figures. The blue numbers above the voltage trace correspond to the cycle period duration of each large cell driver potential and the red numbers correspond to the burst durations.

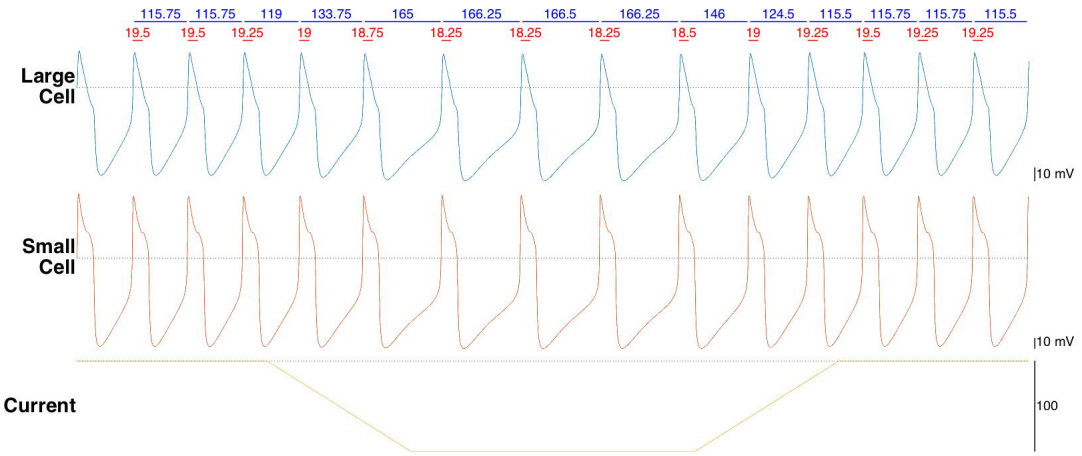

FIGURE 52. Voltage and current traces of Example 5 with $I_s = -100$nA. The x-axis is a unitless time axis showing the same time scale in all figures. The blue numbers above the voltage trace correspond to the cycle period duration of each large cell driver potential and the red numbers correspond to the burst durations.

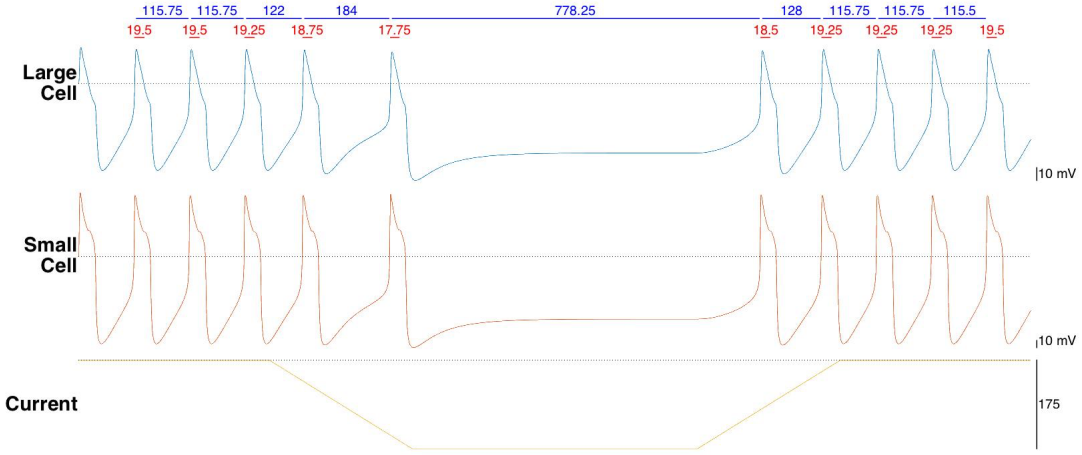

FIGURE 53. Voltage and current traces of Example 5 with $I_s = -175$nA. The x-axis is a unitless time axis showing the same time scale in all figures. The blue numbers above the voltage trace correspond to the cycle period duration of each large cell driver potential and the red numbers correspond to the burst durations.

10.3. **Model Response to Current: Conclusion.**

Similar to the results when current was injected into the decoupled Morris Lecar model, injecting hyperpolarizing and depolarizing currents into the CG model decreases and increases burst frequency, respectively, mimicking **component 2** of the experimentally observed stretch response. This model also reproduces the results found in lab by the current injection experiments, and supports the usability of this coupled model for further manipulations to understand the model network.

It is interesting to note that the currents necessary to increase or decrease the driver potential frequency are 5 times the current injection needed in the decoupled system. What might this suggest?

Additionally, these results support the experimental data, which suggests that the feedback from stretch is not mediated by the opening of a simple stretch-sensitive ion channel since no single current injection led to all stretch response components. This further supports the presence and involvement of the hypothesized mechanosensitive channels TREK and Piezo. We test this hypothesis in the coupled two-cell model in the next section.

Although in this example, the current injection changes the frequency of the burst, only the interburst duration changes, the burst duration remains the same as before and during the current injection. This also suggests that stretch is not mediated by the opening of a simple stretch-sensitive ion channel.

11. Piezo and TREK Channels in Coupled System

11.1. **Model Response to Piezo and TREK channels: Methods.**

Since we know that the coupled Morris Lecar model behaves similarly to the decoupled Morris Lecar model when additional currents are applied, now we can take the mechanosensitive channels: Piezo and TREK, which were previously applied to the decoupled model, and apply them to the coupled model. However, there are multiple ways in which these channels can be incorporated into the model.

Experimental results suggest that after ligating the CG, which removes electrical and chemical signaling from the small cells, the phase delay (**component 1**) and increase in burst duration (**component 3**) upon ramp up and ramp down from stretch, respectively, are lost. These results suggest that the small cells are responsible for influencing the CG's driver potentials to exhibit these components of the stretch response. Since, through this model, we suspect these components of the stretch response are due to the presence of the TREK channel, we hypothesize that the TREK channel is present only in the small cells.

Additionally, an increase in frequency (**component 2**) is observed both when the muscles underlying and surrounding the small cells is kept intact and stretched (causing just the small cells to be actively affected by the stretch) AND when the muscles underlying and surrounding the entire trunk of the CG is kept intact and stretched (causing both the small and large cells to be actively affected by the stretch). We suspect that this component of the stretch response is due to the presence of the Piezo channel. Therefore, we hypothesize that the Piezo channel is present in both cell types.

The equations governing Morris-Lecar dynamics of a two-cell system with Piezo channels in both cells and TREK only in the small cells are as given in Section 4.1, except equations 2 and 3 are changed to equations 15 and 16, respectively, with all other equations unchanged:

$$(14)\quad C\frac{dV^A}{dt} = -g_L^A(V^A - V_L) - g_{Ca}^A M_\infty(V^A - V_{Ca}) - g_K^A W(V^A - V_K) \\ - g_{Syn}^A S_\infty(V^B)(V^A - V_{Syn}) - g_{gap}(V^A - V^B) - I_P$$

$$(15)\quad C\frac{dV^B}{dt} = -g_L^B(V^B - V_L) - g_{Ca}^B M_\infty(V^B - V_{Ca}) - g_K^B W(V^B - V_K) \\ - g_{Syn}^B S_\infty(V^A)(V^B - V_{Syn}) - g_{gap}(V^B - V^A) - I_P - I_T$$

The TREK current I_T is modeled according to equation 5 in Section 7.1 and Piezo current I_P could be modeled according to equations 9 or 12 in Section 8.1.

Example 6

Let's take the same example parameter sets used in Sections 7, 8, 9, and 10, with Piezo channels in both cells and TREK in the small cells only.

11.2. **Model Response to Piezo and TREK channels: Results.**

Figures 54-56 depict the large and small cell voltage traces from Example 6 affected by the Piezo currents, I_P, in both cells and the TREK current, I_T, in the small cells.

Example 6, modeling approach P1

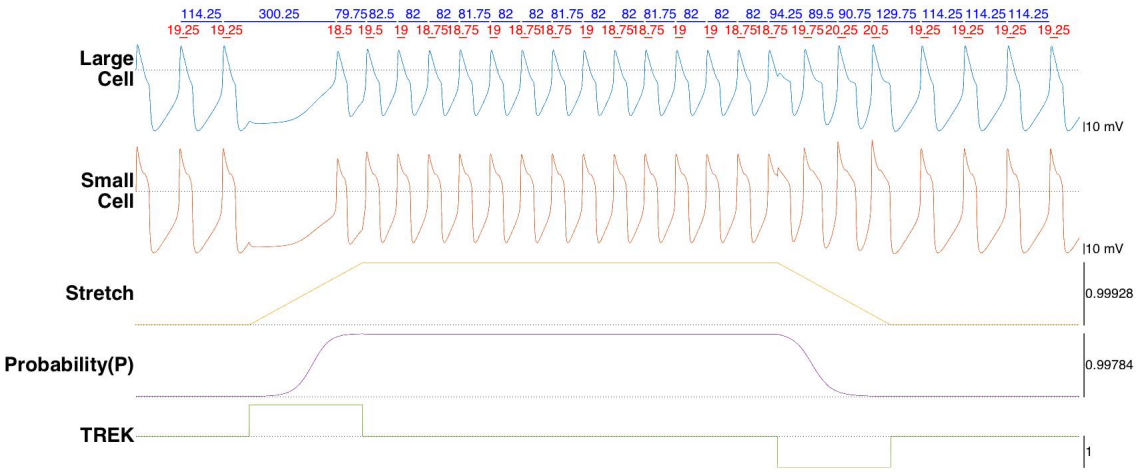

FIGURE 54. Voltage, stretch, and conductance traces of Example 6, modeling approach P1 with $g_P = 3\mu S/cm^2$ and $g_T = 12\mu S/cm^2$. The x-axis is a unitless time axis showing the same time scale in all figures. The blue numbers above the voltage trace correspond to the cycle period duration of each driver potential and the red numbers correspond to the burst durations.

Example 6, modeling approach P2

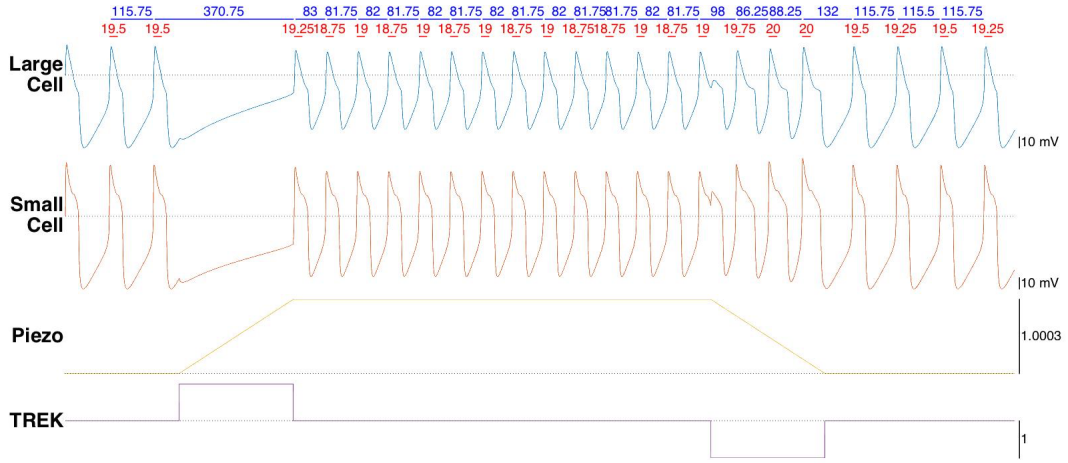

FIGURE 55. Voltage and conductance traces of Example 6, modeling approach P2 with $g_P = 3\mu S/cm^2$ and $g_T = 12\mu S/cm^2$. The x-axis is a unitless time axis showing the same time scale in all figures. The blue numbers above the voltage trace correspond to the cycle period duration of each driver potential and the red numbers correspond to the burst durations.

Example 6, modeling approach P3

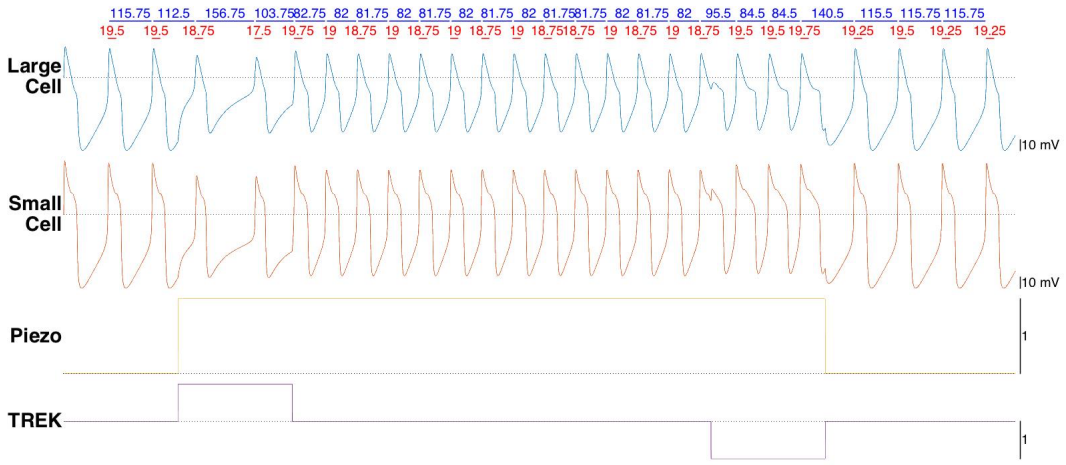

FIGURE 56. Voltage and conductance traces of Example 4, modeling approach P3 with $g_P = 3\mu S/cm^2$ and $g_T = 12\mu S/cm^2$. The x-axis is a unitless time axis showing the same time scale in all figures. The blue numbers above the voltage trace correspond to the cycle period duration of each driver potential and the red numbers correspond to the burst durations.

11.3. Model Response to Piezo and TREK channels: Conclusion.

Recall the experimental data:

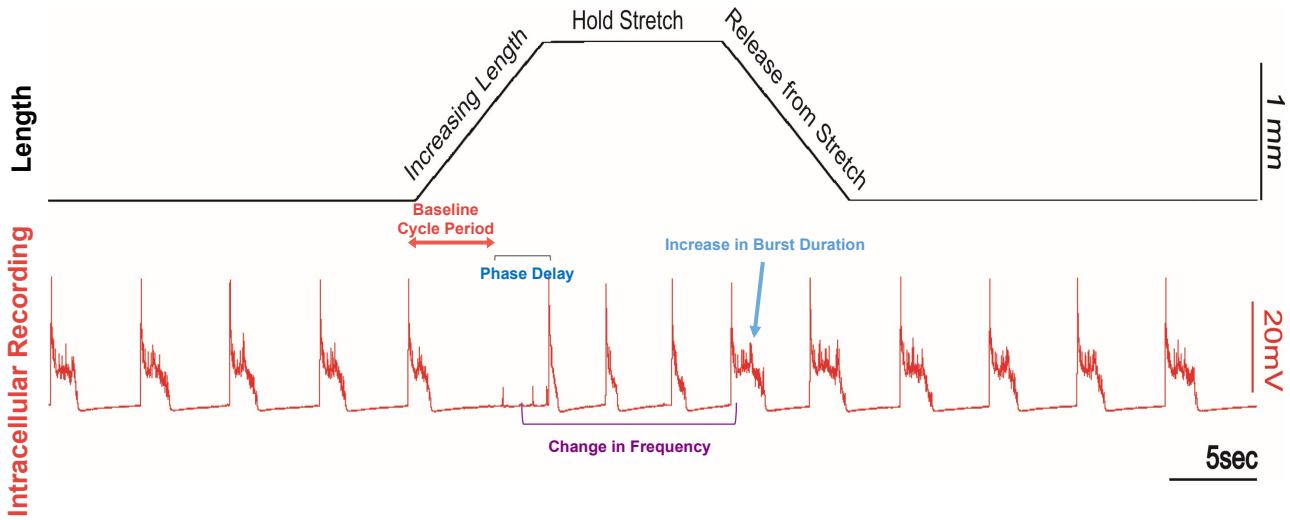

FIGURE 57. Example intracellular recording of a motor neuron during a stretch experiment

It is exciting to see that all three computational models shown by Figures 54-56 in Section 11.2, contain the three components of the stretch response exhibited in experiments, such as the one shown by **Figure 57**. Further analyses of these models are underway in determining which approach to modeling the Piezo current is best suited to ongoing studies. An interesting feature of the two-cell model, that did not occur in the single cell model, is the dramatic increase in burst duration in the small cells during the ramp down of stretch. The model voltage traces show that the increased burst duration is mirrored by the large cells (model motor neurons), but is not captured by our (rather arbitrary) definition of model bursting. Currently, the system is considered to be bursting whenever the voltage V is above 0mV, depicted by the dotted line. Thus, the burst duration is measure as the duration of time the voltage is above the dotted line $V = 0$mV. Although the burst durations measured (depicted in figures 54-56 by the red numbers above the voltage traces) do not change much throughout the stretch experiments, if the dotted line was lowered, the voltage traces would exhibit a clear and defined increase in burst duration during release of stretch. Further work is, therefore, under way to refine the definition of model bursting.

12. Discussion

How cellular properties and coupling parameters influence the steady state behavior of rhythmic networks has been extensively investigated in the mathematical biology literature. Williams et al.(2013) built a simple two-cell computational model of the CG, the CPG of the lobster rhythmic cardiac contraction. This study simulated 15,000 different model networks by randomly selecting the parameter values for 7 maximal conductances, while requiring that the two model cells exhibit spontaneous oscillations in isolation. Of these networks, 13,141 displayed dynamics that resembled CG output. Modulations to this model, or to other Morris Lecar model oscillating networks, to incorporate feedback menchanisms has had little attention [47].

Experimental data suggests the response of the CG neurons to stretch consists of three separate components. With hopes of describing this phenomena, this paper introduces a possible stretch feedback mechanism in a physiologically realistic fashion by incorporating multiple mechanosensitive channels in the previously developed two cell model networks.

Previous studies have described that stretch feedback results from the opening of two types of stretch activated channels: a TREK-1 like mechano-gated K^+ channel and a Piezo-2 like non-specific cation channel [8, 4, 14, 7](Marc W. Miller, Personal communications). Additionally, a non-specific cation stretch channel has been previously modeled as a Voigt element (which consists of a spring in parallel with a dashpot) in series with a nonlinear spring [41].

In our current study, we first decoupled the two-cell Morris Lecar model of the CG by removing electrical and chemical coupling and analyzed the one cell system with these two channels. Through geometric analyses of the phase planes, this study offers explanations for multiple features of the effects of the stretch sensitive channels on the single cell system in terms of the equilibrium points, nullclines and limit cycle trajectories of the model systems. Then, through reintroduction of the second cell with electrical and chemical coupling, and exploration of multiple ways in which the stretch sensitive channels can be incorporated into the coupled model, we finally developed a two-cell model with outputs exhibiting the three components of stretch.

Given that synchrony and feedback within neuronal networks is of interest to mathematical biologists, and because the synchronization patterns of the CG and our model networks have not been thoroughly described before, we investigated how mechanosensitive channels determined

the three components of the stretch feedback mechanisms in the Morris Lecar two-cell model system.

Both computational and experimental studies suggest the complexities of the lobster CG's stretch sensitivity. The model developed in this study is a potential working model of the stretch feedback mechanism within the lobster's CG and supports the presence of at least two types of mechanosensitive channels in the small cells, one of which is also present in the large cells.

The model developed in this paper utilized the coupled Morris-Lecar model of the CG and incorporated two mechanosensitive channels. Based off hypotheses from experimental results, which suggested the placement of these channels, a Piezo Channel was applied to both the large and small cells and a TREK channel in just the small cell. The opening of the TREK channel could be modeled as a step function proportional to the derivative of the slope of the stretch. The opening of the Piezo channel could be modeled in three different ways: it could (1) open via a complex open probability function, (2) open as a function proportional to stretch, or (3) open as a step function. In an example parameter set, all models exhibited the three components of the stretch response, observed experimentally, which supports the plausibility of the model for further analysis.

However, this model also has weaknesses. Firstly, while the model succeeds in exhibiting the increase in burst frequency observed during the hold of stretch, it fails to exhibit the experimentally observed associated decrease in burst duration. Secondly, upon release from the stretch, the increase in burst duration could be more clearly identified if bursting was measured at some voltage below $V = 0$mV (or refined in some other way), as explained in section 11.3. Thirdly, introducing a negative conductance g_T for the TREK channel as stretch ramps down seems biologically implausible at first glance. However, if g_T is interpreted as conductance relative to baseline, rather than absolute conductance, then a novel and reasonable biological interpretation is suggested, as described in Section 7.

This projects is part of a larger team effort to make progress in understanding the complex stretch-feedback mechanism in the lobster CG. This study informs, and is informed by, ongoing and future studies by the team.

For example, the cellular expression and localization of the stretch sensitive channels within the cardiac system will be examined using in situ hybridization and immunohistochemical approaches (Marc W. Miller, Personal communications).

As another example, the Dickinson lab is exploring how neuropeptides applied to the CG might interact with stretch feedback. Specifically, what is the interaction between these neuropeptides and mechanosensitive channels?

Finally, neuronal networks with different cellular and synaptic parameters can produce similar rhythmic outputs. Additionally, ion channel expression/distribution is substantially variable on a preparation-to-preparation basis. Therefore, this model will also be characterized and a sensitivity analysis performed on a population-based scale, as in Williams et al (2103) [47]. Specifically, how much can the parameters of the mechanosensitive channels vary to get the three components of the stretch response?

The following table summarizes potential ranges over which some of the model parameters will be varied over in a population.

Parameters of Couples Morris Lecar System with Piezo and TREK Channels			
Parameter	Variable	Value Used	
Cell surface area, cm^2		0.001	
Total cell capacitance, nF	C	10	
Ca^{2+} reversal potential, mV	V_{Ca}	100	
K^+ reversal potential, mV	V_K	-80	
Leak reversal potential, mV	V_L	-10	
TREK reversal potential, mV	V_T	-80	
PIEZO reversal potential, mV	V_P	10	
Synaptic reversal potential, mV	V_{syn}	-15	
Ca^{2+} half activation slope, mV	V_1	0	
Ca^{2+} current activation slope, mV	V_2	15	
K^+ half activation slope, mV	V_3	0	
K^+ current activation slope, mV	V_4	15	
Synaptic half activation slope, mV	V_5	0	
Synaptic current activation slope, mV	V_6	5	
K^+ current minimum rate constant, ms	ϕ_W	0.002	
Spring constant for linear spring, kPa	k_1	400	
Spring constant for nonlinear spring	k_2	2,200	
Power constant nonlinear spring	n	2	
Dashpot constant,kPa-ms	B	12,000	
Boltzmann constant (linear)	k_b	106	
Sensitivity constant (linear), kPa^{-1}	s	2.77	
Power constant (linear)	q	1	
Parameter	Variable	Min. Value Used	Max. Value Used
Ca^{2+} current maximal conductance, $\mu S/cm^2$	g_{Ca}	0	100
K^+ current maximal conductance, $\mu S/cm^2$	g_K	0	100
Ca^{2+} current maximal conductance, $\mu S/cm^2$	g_L	0	10
Chemical synaptic strength, $\mu S/cm^2$	g_{syn}	0	50
Electrical coupling strength, $\mu S/cm^2$	g_{gap}	5	40
TREK current maximal conductance, $\mu S/cm^2$	g_T	1	60
PIEZO current maximal conductance, $\mu S/cm^2$	g_P	1	30
Tension conversion factor	m	0	61.6

13. Appendix

XPP Code:

```
coupled system differential equations;
dVA/dt = .1*(-gLA*(VA-VL)-gCA*Minf(VA)*(VA-VC)-gKA*WA*(VA-VK)-gSA*Sinf(VB)*(VA-
VS)-ggap*(VA-VB)-Po(epsilon2)*(VA-VP))/C
dVB/dt = .1*(-gLB*(VB-VL)-gCB*Minf(VB)*(VB-VC)-gKB*WB*(VB-VK)-gSB*Sinf(VA)*(VB-
VS)-ggap*(VB-VA)-Po(epsilon2)*(VB-VP)-stretchT(t)*(VB-VT))/C
dWA/dt = 10*(Winf(VA)-WA)/(tauW(VA))
dWB/dt = 10*(Winf(VB)-WB)/(tauW(VB))
Minf(V) = 0.5*(1+tanh((V-V1)/V2))
Winf(V) = 0.5*(1+tanh((V-V3)/V4))
Sinf(V) = 0.5*(1+tanh((V-V5)/V6))
tauW(V) = 1/(phiW*cosh((V-V3)/(2*V4)))
TREK CHANNEL ApproachT1;
IT = stretchT(t)*(VB-VT)
stretchT(t) = gT*heav(t-first)*heav(second-t)*(alpha)+heav(t-second-0.001)*heav(third-t)*(0)+heav(t-
third-.001)*heav(fourth-t)*(-alpha)
param gT=12, VT=-80
PIEZO CHANNEL ApproachP1:
depsilon/dt = ed
depsilon2/dt = (k1*epsilon-k1*(epsilon2)-k2*(epsilon2)^(n+1))/(B) + ed
ed = heav(t-first)*heav(second-t)*(alpha/ts)+heav(t-second-0.001)*heav(third-t)*(0)+heav(t-
third-.001)*heav(fourth-t)*(-alpha/ts)
param k1=400,B=12000, n=2,k2=22000
Po(epsilon2)=gP*((1+kb*exp(-som*(k2*(epsilon2)^(n + 1))))^( - 1))
param kb=106, som=0.045, gP=6,q=1,VP=10
STRETCH PARAMETERS
param alpha=1,
param param first=300,third=1700,ts=300
second = first+ts
fourth = third+ts
default parameters
param VC=100,VK=-80,VL=-10,C=10,V1=0,V2=15,V3=0,V4=15,V5=0,V6=5,phiW=0.002,VS=-
15
param gCA=23, gCB=67, gKA=50, gKB=81, gSA=36,gSB=22, ggap=24, gLA=1, gLB=3
@ xp=t,yp=VA,xlo=0,xhi=3000,ylo=-70,yhi=70
@ dt=.25,total=2500,bounds=10000,maxstore=30000
```

14. Acknowledgements

I would like to thank my friends and family for their wonderful support throughout this year while I completed this project. I would also like to thank past and present Dickinson lab members for their support and the lab's experimental data used for the completion of this project. I would like to extend a special thanks to Matt Gorroff, with whom I have worked closely with throughout the year and to Xian Qu, who has provided me with immense experimental support. Thank you to those who read my thesis, specifically my readers Professors Adam Levy, Michael King, and Charles Cunningham. I greatly appreciate your comments, feedback, and guidance.

I most importantly need to thank Professors Mary Lou Zeeman, Patsy Dickinson, Olaf Ellers, and Amy Johnson, my advisors, for providing this incredible opportunity and for supporting the research process to make this project possible. Your encouragement and guidance through questions and challenges I faced motivated me to persevere and encouraged me. The collaboration between biology and mathematics pushed me to think deeply and creatively. Your passion for research is truly inspiring.

This research was supported by NSF IOS-1121973, INBRE, Doherty Coastal Fellowship, and Irving fund.

References

[1] J. Albert, C.J. Lingle, E. Marder, and M.B. O'Neil. A gaba-activated chloride-conductance not blocked by picrotoxin on spiny lobster neuromuscular preparations. *J. Pharmac.*, 87:771–779, 1986.

[2] J.S. Alexandrowicz. Innervation of the heart of the crustacea. i. decapoda. *Q. J. Microsc. Science*, 75:182–249, 1932.

[3] M. Anderson and I.M. Cooke. Neural activation of the heart of the lobster, homarus americanus. *J. Exp. Biol.*, 55:449–468, 1971.

[4] M. Schmidt T.J. Earley S. Ranade M.J. Petrus A.E. Dubin B. Coste, J. Mathur and A. Patapoutian. Piezo1 and piezo2 are essential components of distinct mechanically-activated cation channels. *Science*, 330(6000):55–60, 2010.

[5] S.N. Bagriantsev, E.O. Gracheva, and P.G. Gallagher. Piezo proteins: Regulators of mechanosensation and other cellular processes. *J. Biol. Chem*, 289(46):31673–31681, 2014.

[6] I.M. Cooke. Reliable, responsive pacemaking and pattern generation with minimal cell numbers: the crustacean cardiac ganglion. *Biol. Bull.*, 202:108–136, 2002.

[7] B. Coste, B. Xiao, J.S. Santos., R. Syeda, J. Grandl, K.S. Spencer, S. Kim, M. Schmidt, A.E. Dubin J. Mathur, M. Montal, and A. Patapoutian. Piezos are pore-forming subunits of mechanically activated channels. *Nature*, 483(7388):176–181, 2012.

[8] P. Hunter S. Smaill D.A. Saint D. Kelly, L. Mackenzie. Gene expression of stretch-activated channels and mechanoelectric feedback in the heart. *Clin. Exp. Pharmacol. Physiol.*, 33(7):642–648, 2006.

[9] F. Delcomyn. Neural basis of rhythmic behavior in animals. *Science*, 210:492–498, 1980.

[10] P.S. Dickinson. Neuromodulation of central pattern generators in invertebrates and vertebrates. *Curr. Opin. Neurobiol.*, 16:604–614, 2006.

[11] J. Chemin T. Suchyna E. Honore, A. Patel and F. Sachs. Desensitization of mechano-gated k2p channels. *J. Exp. Biol.*, 84:89–101, 2006.

[12] C. Eder, R. Klee, and U. Heinemann. Involvement of stretch-activated cl2 channels in ramification of murine microglia. *J. Neurosci.*, 18(18):7127–7137, 1998.

[13] C. Erxleben. Stretch-activated current through single ion channels in the abdominal stretch receptor organ of the crayfish. *J. Gen. Physiol.*, 94:1071–1083, 1989.

[14] M. Fink, F. Duprat, F. Lesage, R. Reyes, G. Romey, C. Heurteaux, and M. Lazdunski. Cloning, functional expression and brain localization of a novel unconventional outward rectifier k+ channel. *EMBO J.*, 15:6854–6862, 1996.

[15] J.M. Goaillard, A.L. Taylor, D.J Schulz, and E. Marder. Functional consequences of animal-to-animal variation in circuit parameters. *Nat. Neurosci.*, 12:1424–1430, 2009.

[16] M.F. Goy. Nitric oxide: an inhibitory retrograde modulator in the crustacean heart. *Comp. Biochem. Physiol.*, 142:151–163, 2005.

[17] N. Hagiwara. Stretch-activated anion currents of rabbit cardiac myocytes. *J. Physiol.*, 456:285–302, 1992.

[18] K. Harmon. Cellular mechanism mediating stretch feedback in the heart of the american lobster, homarus americanus. An Honors Project for the Program of Neuroscience, 2014.

[19] D.K. Hartline. Integrative neurophysiology of the lobster cardiac ganglion. *Am. Zool.*, 19(1):53–65, 1979.

[20] D.K. Hartline. Integrative neurophysiology of the lobster cardiac ganglion. *Am. Zool.*, 19(1):53–65, 1979.

[21] E. Honore. The neuronal background k2p channels: focus on trek1. *Nature Reviews Neuroscience*, 8:251–261, 2007.

[22] S.L. Hooper. Phase maintenance in the pyloric pattern of the lobster (panulirus interruptus) stomatogastric ganglion. *J. Comput. Neurosci.*, 4:191–205, 1997.

[23] S.L. Hooper. The pyloric pattern of the lobster (panulirus interruptus) stomatogastric ganglion comprises two phase-maintaining subsets. *J. Comput. Neurosci.*, 4:207–219, 1997.

[24] G.M. Hughes and A.G. Wiersma. The co-ordination of swimmeret movements in the crayfish, procambarus clarkii (girard). *J. Exp. Biol*, 37(4):657–670, 1960.

[25] J.Boistel and P. Fatt. Membrane permeability change during inhibitory transmitter action in crustacean muscle. *J. Physiol.*, 144:176–191, 1958.

[26] E.A. Kravitz, S. Glusman, R.M. Harris-Warrick, M.S. Livingstone, T. Schwarz, and M.F. Goy. Amines and a peptide as neurohormones in lobsters: actions on neuromuscular preparations and preliminary behavioural studies. *J. Exp. Biol.*, 89:159–175, 1980.

[27] S.W. Kuffler and C. Eyzaguirre. Synaptic inhibition in an isolated nerve cell. *J. Gen. Physiol.*, 39(1):155–184, 1955.

[28] T. Kuramoto. Cardiac activation and inhibition involved in molting behavior of a spiny lobster. *Experientia.*, 49:682–685, 1993.

[29] T.J. Lewis and J. Rinzel. Dynamics of spiking neurons connected by both inhibitory and electrical coupling. *J. Comput. Neurosci.*, 14(3):283–309, 2003.
[30] A. Mahadevan, R. Rhyne J. Lappe, N. Cruz-Bermudez, E. Marder, and M. Goy. Nitric oxide inhibits the rate and strength of cardiac contractions in the lobster homarus americanus by acting on the cardiac ganglion. *J. Neurosci.*, 24:2813–2824, 2004.
[31] E. Mayeri. Functional organization of the cardiac ganglion of the lobster. *J. Gen. Physiol.*, 62:448–472, 1973.
[32] D.L. Mykles. The mechanism of fluid absorption at ecdysis in the american lobster, homarus americanus. *J. Exp. Biol.*, 84:89–101, 1980.
[33] J.L Ransdell, S.S. Nair, and D.J. Schulz. Rapid homeostatic plasticity of intrinsic excitability in a central pattern generator network stabilizes functional neural network output. *J. Neurosci.*, 32:9649–9658, 2012.
[34] J.L Ransdell, S.S. Nair, and D.J. Schulz. Neurons within the same network independently achieve conserved output by differentially balancing variable conductance magnitudes. *J. Neurosci.*, 33(24):9950–9956, 2013.
[35] J.L. Ransdell, N.L. West S. Temporal, M.L. Lerer, and D.J. Schulz. Characterization of inward currents and channels underlying burst activity in motor neurons of the crab cardiac ganglion. *J. Neurophysiol.*, 110(1):42–54, 2013.
[36] S. Simrick R.F. Schindler, K. Poon and T. Brand. The popeye domain containing genes: essential elements in heart rate control. *Cardiovasc. Diagn. Ther.*, 2(4):308–319, 2012.
[37] N.L. Scholz, J. DeVente J.S. Labenia, K. Graubard, and M.F. Goy. Expression of nitric oxide synthase and nitric oxide-sensitive guanylate cyclase in the crustacean cardiac ganglion. *Comp. Neurol.*, 454:158–167, 2002.
[38] D.J. Schulz, J.M. Goaillard, and E. Marder. Variable channel expression in identified single and electrically coupled neurons in different animals. *Nat. Neurosci.*, 9:356–362, 2006.
[39] D.J Schulz, J.M. Goaillard, and E. Marder. Quantitative expression profiling of identified neurons reveals cell-specific constraints on highly variable levels of gene expression. *Proc. Natl. Acad. Sci. USA*, 104:13187–13191, 2007.
[40] F.K. Skinner, N. Kopell, and E. Marder. Mechanisms for oscillation and frequency control in reciprocally inhibitory model neural networks. *J. Comput. Neurosci.*, 1(1):69–87, 1994.
[41] C. Swerup and B. Rydqvist. A mathematical model of the crustacean stretch receptor neuron. biomechanics of the receptor muscle, mechanosensitive ion channels, and macrotransducer properties. *J. Neurophysiol.*, 76:2211–2220, 1996.
[42] L.S. Tang, M.L. Goeritz, J.S. Caplan, A.L. Taylor, M. Fisek, and E. Marder. Functional consequences of animal-to-animal variation in circuit parameters. *PLoS. Biol*, 8:e1000469, 2010.
[43] K. Tazaki and I.M. Cooke. Ionic bases of slow, depolarizing responses of cardiac ganglion neurons in the crab, portuus sanguinolentus. *J. Neurophysiol.*, 42(4):1022–1047, 1979.
[44] K. Tazaki and I.M. Cooke. Isolation and characterzation of slow, depolarizing responses of cardiac ganglion neurons in the crab, portuus sanguinolentus. *J. Neurophysiol.*, 42(4):1000–1021, 1979.
[45] K. Tazaki and I.M. Cooke. Spontaneous electrical activity and interaction of large and small cells in cardiac ganglion neurons in the crab, portuus sanguinolentus. *J. Neurophysiol.*, 42(4):975–999, 1979.
[46] J.L. Wilkens. Re-evaluation of the stretch sensitivity hypothesis of crustacean hearts: hypoxia, not lack of stretch, causes reduction in heart rate of isolated hearts. *J. Exp. Biol.*, 176:223–232, 1993.
[47] A.H. Williams, M.A. Kwiatkowski, A.L. Mortimer, M. Zeeman E. Marder, and P.S. Dickinson. Animal-to-animal variability in the phasing of the crustacean cardiac motor pattern: an experimental and computational analysis. *J. Neurophysiol.*, 103:2451–2465, 2013.